Chapter 6
Stiffener-Enhanced Steel–Concrete-Steel Sandwich Beam and Panel Under Impact

6.1 Introduction

Steel–concrete-steel (SCS) sandwich structure is composed of two external steel plates and a concrete core. The mechanical shear connectors are usually employed to bond the steel plates to concrete core and provide longitudinal and transverse shear resistance as well as prevent separation between the external steel plates and concrete core. The SCS sandwich structures were found to outperform traditional reinforced concrete structures in terms of superior strength, ductility and spalling protection (Wang et al. 2016), which promoted its application in resisting potential impact load. The mechanical shear connector was proven to be of significance in ensuring structural integrity and improving impact resistance of the SCS sandwich structure (Liew et al. 2009). Hence, several types of shear connectors have been developed in recent decades, including headed shear stud (Oduyemi and Wright 1989), Bi-steel (Foundoukos 2005), angle shear connector (Guo et al. 2020), interlocked J-hook connector (Liew and Sohel 2009), bolt connector (Yan et al. 2020a) and enhanced C-channel connector (Yan et al. 2020c, d). As illustrated in Fig. 6.1, a new SCS sandwich structure enhanced with stiffeners in the tension plate, namely stiffener-enhanced SCS (SESCS) sandwich structure, was proposed to improve the impact resistance of the SCS sandwich structure with traditional bolt connectors, and its impact behavior was studied and presented in this chapter.

Owing to the desirable ductility and strength of the SCS sandwich structure, it was widely employed to resist variant loads, including static, impact and blast loads (Wang et al. 2016; Nie et al. 2014; Sohel and Liew 2014; Liew et al. 2015). The interfacial bonding strength, which is usually achieved via shear connectors and cohesive material, is of significance for bonding the concrete core to faceplates and assuring the composite action of SCS sandwich structures. In the past, headed studs were usually employed to be welded to the two faceplates for preventing separation and longitudinal slip between faceplates and concrete core (Thang et al. 2016; Dogan and Roberts 2012; Subedi and Coyle 2002) owing to its low costing and easy fabrication. However, the headed studs were found to be weak in preventing tensile

Y. Wang et al., *Innovations in Impact and Blast Protections*,
https://doi.org/10.1007/978-981-19-4375-1_6

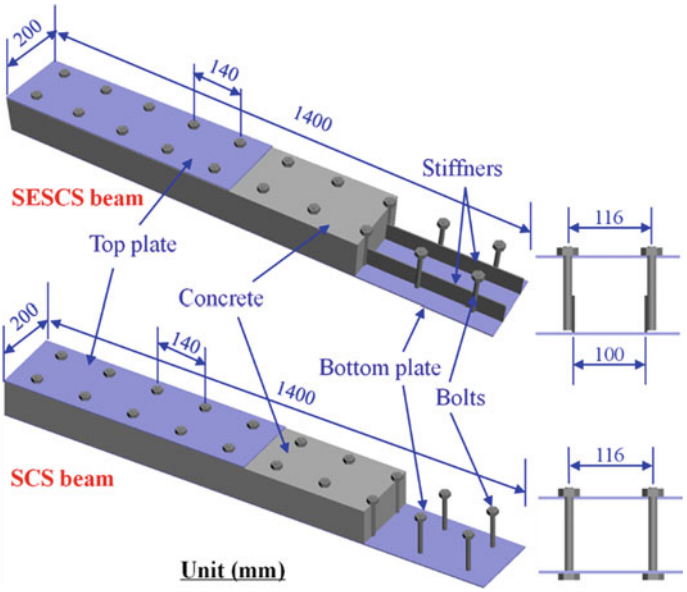

Fig. 6.1 General illustration of SESCS and SCS sandwich beams, reprinted from Wang et al. (2021), copyright 2022, with permission from Elsevier

separation of faceplates (Liew et al. 2009), since they were embedded into the concrete core separately, and the tensile force was transferred through the concrete core. In addition, steel angles could also be welded to the two faceplates of SCS sandwich structures to provide longitudinal and transverse shear resistance (Shariati et al. 2012, 2013, 2016). Similar to the headed shear studs, the separation between faceplates and concrete core could be observed owing to the shallowly embedding depth of steel angles (Yan et al. 2015). In order to improve the structural integrity of the SCS sandwich structure and prevent separation of faceplates, several "through-through" types of shear connectors have been proposed. Xie et al. (2007) developed a friction-welded shear connector, which allowed straight steel bar connectors being connected to the two faceplates via friction welding (Xie et al. 2007; Clubley et al. 2003). Hence, the tensile separation of faceplates could be resisted via developing tensile force in the steel bar connectors. Bolts could be another type of shear connectors with desirable bonding strength and easy fabrication (Yan et al. 2020b). Recently, the interlocked J-hook connectors were developed by Liew and Sohel (2009), and they were found to be an effective bonding method for SCS sandwich structures. The combination of headed shear studs and tie bars were also employed for SCS sandwich slabs to yield desirable longitudinal and transverse shear resistance (Wang et al. 2020). More recently, an enhanced C-channel connector was developed by Yan et al. (2020a, b, c, d), and the strong tension separation resistance of faceplates from concrete core and faceplate-concrete interfacial shear resistance could be achieved when using the novel enhanced C-channel connectors (Yan et al. 2020c).

Most of the previous studies have been focused on the behaviors of SCS sandwich structures subjected to static or quasi-static loading. Few studies have been focused on the impact responses of SCS sandwich structures. Experimental studies were conducted by Sohel et al. (2003) to investigate the impact behaviors of SCS sandwich beams with angle connectors, and tension separation of faceplates were observed for most of the test specimens owing to the weak tension separation resistance of angle connectors. The J-hook connectors were proposed for enhancing the tension separation resistance of faceplates, and the improved impact resistant performance of SCS sandwich structures with J-hook connectors could be observed (Liew et al. 2009, 2015; Sohel and Liew 2014). It was also found by Liew et al. (2009) that the composite action of SCS sandwich beams could be enhanced when fiber reinforced concrete was employed for the core material. By employing the experimental, numerical and analytical approaches, the dynamic response behaviors of SCS sandwich beams with J-hook connectors were studied (Liew et al. 2009, 2015), and the developed analytical model was found to be accurate in predicting the impact force and displacement responses of the SCS sandwich beams (Liew et al. 2009). With regard to the impact behaviors of axially-restrained SCS sandwich panels without shear connectors, the highly ductile response could be observed with initial flexural response and following tensile membrane stretching of faceplates (Remennikov and Kong 2012; Remennikov et al. 2013). The enhanced blast resistant performance of axially-restrained non-composite SCS sandwich panels via developing tensile membrane stretching were also demonstrated by Wang et al. (2015a). The SCS sandwich structures could be subjected to the combination of axial compressive pre-load and lateral impact load when they were employed as walls and meanwhile experienced an accidental collision. Experimental studies were conducted on the impact responses of SCS sandwich panels with axial compressive pre-load. The combination of local indentation and global flexure was observed (Zhao and Guo 2018; Zhao et al. 2018). In addition, an analytical model was also developed for predicting the impact-induced displacement response of the SCS sandwich panel (Guo and Zhao 2019a, b). On employing bolt connectors, the impact responses of curved SCS sandwich shells were studied by Yan et al. (2020a, b, c, d). The local deformation was found to be dominated, and the bolt connectors have shown a high tension separation resistance of faceplates.

In this chapter, a new SESCS sandwich structure was proposed to resist impact loading. Drop-weight impact tests on SESCS sandwich beams and panels were conducted to reveal their behaviors under low-velocity impact loading. In addition, the numerical studies were also conducted to further reveal the impact responses of SESCS sandwich structures. An analytical model was developed for predicting the displacement response of the SESCS sandwich beam under impact loading.

6.2 SESCS Sandwich Beam Under Impact

6.2.1 Experimental Study

6.2.1.1 Specimens

The SESCS sandwich beams designed for the drop-weight impact tests are shown in Fig. 6.1. The two stiffeners were welded to the tension plate (bottom plate) of the SCS sandwich beam first (Fig. 6.2b). Subsequently, one end of the bolt was welded to the stiffener (Fig. 6.2b) with the other being fastened to the compression plate (top plate) through nuts, as shown in Fig. 6.2c. Finally, concrete casting was implemented (Fig. 6.2d), and the specimens were curing for at least 28 days before test. There were seven SCS sandwich beams being fabricated for the impact tests, and all the specimens shared the same length and width of 1400 and 200 mm, respectively. The 12 mm-diameter bolts were employed for all the specimens with spacing of 140 mm. The stiffeners of all the SESCS sandwich beams shared the same dimension of 1400×50×3.52 mm. There were six SESCS sandwich beams being designed, and the variant parameters included faceplate thickness, concrete core thickness and impact velocity. In addition, one SCS sandwich beam with traditional bolt connectors was also fabricated for comparison and confirming the enhanced impact resistance of the SESCS sandwich beam. As shown in Fig. 6.1, the two

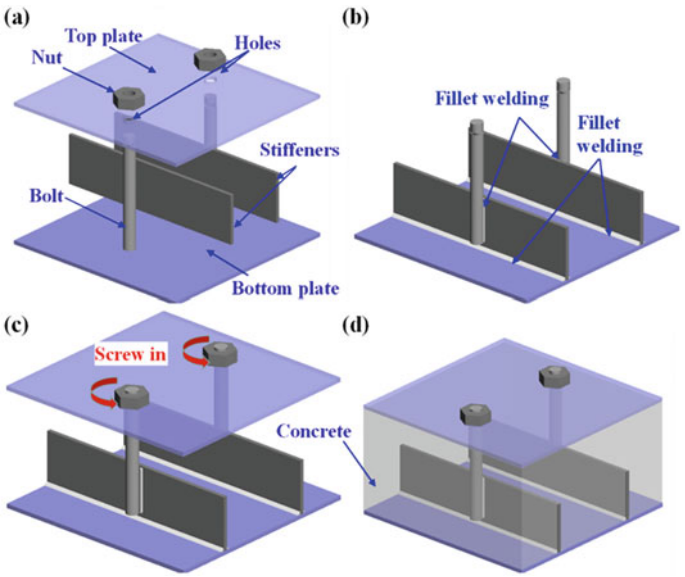

Fig. 6.2 Fabrication process of the SESCS sandwich beam: **a** Components, **b** Welding stiffener and bolt, **c** Assembling two plates by bolt, **d** Concrete casting, reprinted from Wang et al. (2021), copyright 2022, with permission from Elsevier

Table 6.1 Summary of test specimens for SESCS sandwich beam (unit: mm)

Specimen	t_c	h_c	t_t	H	V (m/s)
Bs4-100	3.52	100	3.52	1200	4.62
Bs3-100	2.84	100	2.84	1200	4.68
Bs5-100	4.46	100	4.46	1200	4.72
Bs4-120	3.52	120	3.52	1200	4.66
Bs4-150	3.52	150	3.52	1200	4.65
Bb4-100	3.52	100	3.52	1200	4.68
Bs4-100 V	3.52	100	3.52	1400	5.09

Note t_c, h_c, and t_t–Thicknesses of top plate, concrete core and bottom plate; H, V–Drop height and velocity of the hammer; Bs and Bb stand for the SCS sandwich beam with stiffeners in tension plate and bolt connectors, respectively

Table 6.2 Material parameters of mild steel, bolt and concrete

Mild steel	E_s (GPa)	f_y (MPa)	f_u (MPa)
$t_p = 2.84$ mm	202	323	455
$t_p = 3.52$ mm	205	286	404
$t_p = 4.46$ mm	210	274	377
Bolt	200	640	800
Concrete	E_c (GPa)	f_c (MPa)	μ
–	29	45	0.211

Note E_s, f_y, f_u–Young's modulus, yield stress and ultimate stress of steel; t_p–steel plate thickness; E_c, f_c, μ–Elastic modulus, compressive stress and Poisson's ratio of concrete

faceplates were punched with holes for the bolts being through the faceplates, and the nuts were employed for fastening the two faceplates. Finally, concrete casting was implemented. The bolt employed for the SCS sandwich beam shared the same diameter and strength with the SESCS sandwich beam. The information of the test specimens are given in Table 6.1. The mild steel was employed for the faceplates and stiffeners. The concrete core was normal weight concrete with compressive strength of 45 MPa. The material properties of mild steel, bolts and concrete employed for fabricating the sandwich beams are presented in Table 6.2.

6.2.1.2 Test Setup and Instrumentation

An instrumented drop-weight impact test machine was employed to conduct the impact tests on the SCS sandwich beams, and Fig. 6.3 presents the test setup and instrumentation. As illustrated in Fig. 6.3b, the SCS sandwich beam was simply supported on the two round bars with clear span to be 1200 mm. The drop weight of all the test specimens is 400 kg, and the drop heights and measured impact velocities

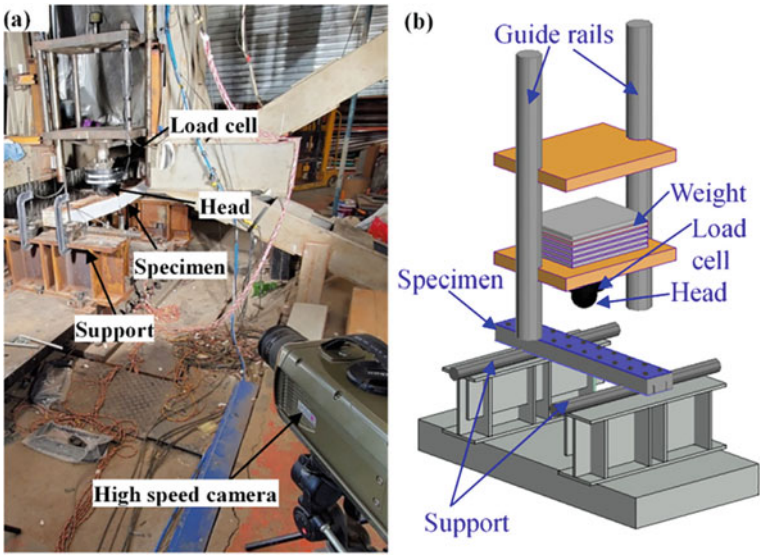

Fig. 6.3 Test setup and instrumentation: **a** photograph and **b** schematic view, reprinted from Wang et al. (2021), copyright 2022, with permission from Elsevier

are given in Table 6.1. The hemispherical hammer head with the diameter of 200 mm was employed for all the test specimens. To measure the impact force, a dynamic load cell with 2000-kN-loading capacity was embedded in the hammer head. Three potentiometers were placed below the specimen to record the deflections, with one at the mid-span and the other two at the quarter-spans. All the readings from the load cell and potentiometers were recorded by a data logger with the sampling rate of 100 kHz. In addition to the measurements of force and displacement, a high-speed camera was utilized for capturing movement of the hammer and deformation of the specimen with the speed of 3000 frames per second.

6.2.1.3 Test Results and Discussions

Failure Modes

The failure modes of the test specimens are presented in Fig. 6.4, and typical flexural failure mode is observed for all the seven SCS sandwich beams with plastic hinges at their mid-spans. The large impact-induced sagging moment at the mid-span results in the appearance of vertical cracks whose widths exhibit largest value near the bottom surface and gradually reduces when they approaches the neutral axis. In addition, sagging moment also causes concrete crushing at compression zone for the six SESCS sandwich beams. The observed cracking patterns of the SESCS sandwich beam are consistent with those of an under-reinforced concrete beam with typical

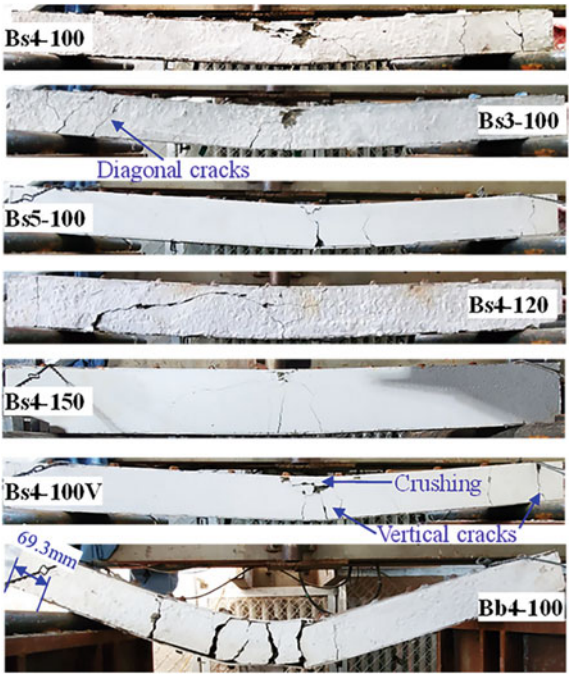

Fig. 6.4 Failure modes of SESCS sandwich beams, reprinted from Wang et al. (2021), copyright 2022, with permission from Elsevier

flexural failure. There is no buckling and separation of the top plate being observed for the six SESCS sandwich beams, which demonstrates the effectiveness of employing bolts for fastening the top plate to concrete core. Besides the concrete crushing and cracking observed near the mid-span of the beam, the vertical and diagonal cracks are also observed for the test beams near only one end of the beam, which results in the slippage between the bottom plate and concrete core occurred at these ends with cracks. It is observed after the impact test that all the beams (except for Bs4-150) exhibit some slippages between the bottom plate and concrete core at only one end of the beam, and the values of slippage are presented in Table 6.3. It is noted that increasing bottom plate thickness and reducing concrete core thickness results in larger value of slippage. In addition, the comparison of slippages of Bs4-100 and Bs4-100 V reveals that larger deformation also causes larger value of slippage. One SCS sandwich beam with bolt connectors (Bb4-100) was also tested under the same impact load as the SESCS sandwich beam. However, it failed to resist the impact load and experienced very large deformation (i.e., the mid-span displacement is greater than 135.7 mm). All the bolts in the left half-span of Bb4-100 exhibited shear failure after impact test, which resulted in large slippage between the bottom plate and concrete core in the left half-span with slippage value exceeding 69.3 mm. The comparison of Bs4-100 and Bb4-100 reveals that the impact resistance of the SCS sandwich beam can be significantly improved by employing stiffeners in the tension plate. It should be mentioned that a temporary rigid support was placed below the beam before the test to prevent falling of the beam from the two round bar supports and protect the

Table 6.3 Summary of test results for SESCS sandwich beam

Specimen	F_{max} (kN)	F_m (kN)	D_{mm} (mm)	D_{qm1} (mm)	D_{qm2} (mm)	S_s (mm)
Bs4-100	181.12	103.63	38.53	23.89	20.03	5.29
Bs3-100	178.36	96.12	42.68	22.37	23.81	5.15
Bs5-100	175.31	103.92	38.92	26.49	19.59	9.23
Bs4-120	204.91	131.49	29.99	15.25	17.27	4.17
Bs4-150	262.14	206.34	18.27	9.69	9.42	0
Bs4-100 V	182.00	102.14	44.69	26.93	24.04	7.00
Bb4-100	–	–	> 135.73	–	–	> 69.3

Note F_{max}, F_m–Peak impact force and post-peak mean force; D_{mm}, D_{qm1}, D_{qm2}–Maximum values of mid-span and quarter-span displacement; S_s–Value of slippage

instrumentations. The specimen Bb4-100 was found to touch the temporary rigid support during the impact test. Hence, the measurements for Bb4-100 are not the real values, and the real ones should be larger than the measurements.

Figure 6.5 presents the impact process of the specimen Bs4-100 V obtained from the high-speed camera, and the failure mode and cracking evolution of the SESCS sandwich beam can be observed. The first vertical crack of the concrete core occurs at 2.3 ms near the mid-span. With continuous impact of the hammer, the shear force-induced diagonal crack near the support occurs at 4.0 ms. Subsequently, the crushing of concrete at compression zone occurs at 5.0 ms. The sequential occurrence of vertical crack at tension zone and concrete crushing at compression zone is consistent with the cracking patterns of an under-reinforced concrete beam with typical flexural failure. This also indicates that the crushing of concrete at compression zone is mainly caused by the sagging moment. With further impact of the hammer, the concrete crushing zone exhibits continuous increase in area, and the vertical and diagonal cracks also exhibit increase in their widths and numbers before the beam reaching its maximum deflection at 17.7 ms.

The normalized deformed shapes of the SESCS sandwich beams are presented in Fig. 6.6a, b, in which the ratios of δ/δ_{max} were measured from the top plate and bottom plate, respectively, after the impact test. Herein, δ is the measured vertical distance between the measured point and the point of the top (or bottom) plate at the support after the impact tests, and δ_{max} is the maximum value of δ along the span direction of the beam. The normalized deformed profiles of all the test SESCS sandwich beams exhibit bi-linear shapes with peak values of δ/δ_{max} at their mid-spans, which further confirms the flexural deformation modes of the SESCS sandwich beams.

Load and Displacement Response

Figure 6.7 presents the typical impact force–time curve of the SESCS sandwich beam (Bs4-100), together with its mid-span and hammer displacements versus time curves. Three stages of the SESCS sandwich beam under impact load can be identified based

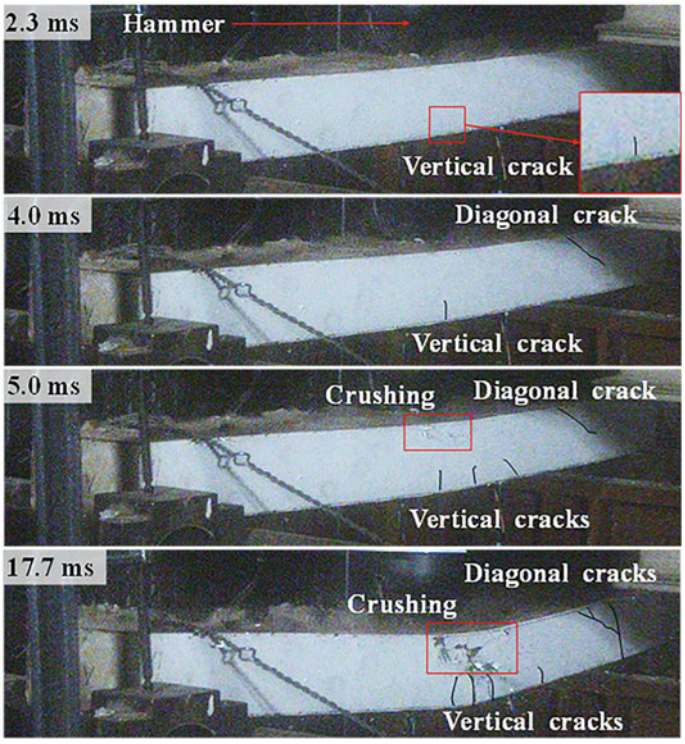

Fig. 6.5 Impact process of the specimen Bs4-100 V, reprinted from Wang et al. (2021), copyright 2022, with permission from Elsevier

on the impact force and displacement response histories in Fig. 6.7, including inertial, loading and unloading stages, as observed by other researchers (Zhao and Guo 2018; Yan et al. 2020a, b, c, d). The impact force exhibits rapid and continuous increase to the peak value once the hammer strikes the beam. The first peak impact force, which is generally larger than the resistance of the beam, is induced by inertial effect at the initial impact stage. This peak impact force cannot represent the real load carried by the beam, and its value is governed by many factors, e.g., local contact stiffness, beam mass, drop weight and height (or impact velocity), etc. In addition, the maximum local indentation depth occurs at the inertial stage owing to the large first peak impact force. At inertial stage, the hammer displacement increase faster as compared to mid-span displacement of the beam, and the displacement difference between the two, which can generally represent the local indentation depth, reaches a constant value at the end of inertial stage. This also indicates that the maximum local indentation depth occurs at the inertial stage. In the loading stage, the beam continuously moves downwards, sharing the identical velocity to the drop hammer. Hence, the inertial effect is insignificant, and the impact force can generally represent the real load carried by the beam. The impact force nearly exhibits a constant value with fluctuation

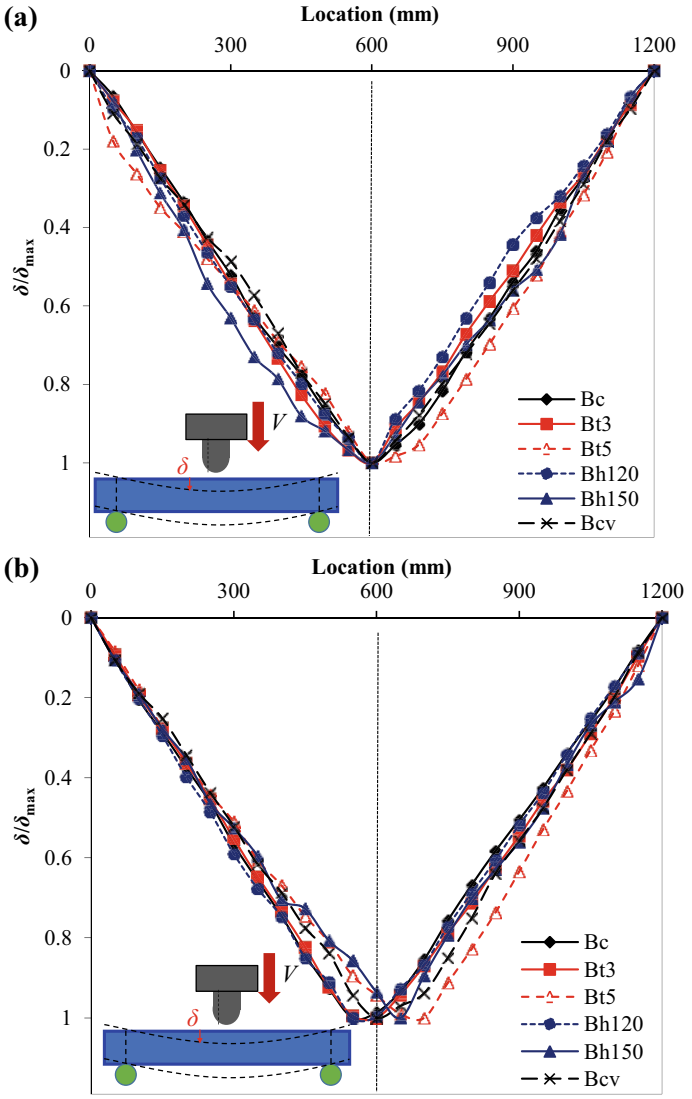

Fig. 6.6 Normalized deformed shapes of SESCS sandwich beams: **a** Top surface, **b** Bottom surface, reprinted from Wang et al. (2021), copyright 2022, with permission from Elsevier

of the curve in the loading stage. When the beam reaches its maximum displacement, the hammer and beam start to rebound together. It enters unloading stage, and both the hammer and mid-span displacements exhibit continuous decrease. In addition, the impact force also decreases, which can be attributed to reduced contact area between the hammer and beam caused by higher rebound speed of the hammer as compared to the beam. The impact force drops to zero when the hammer completely separates

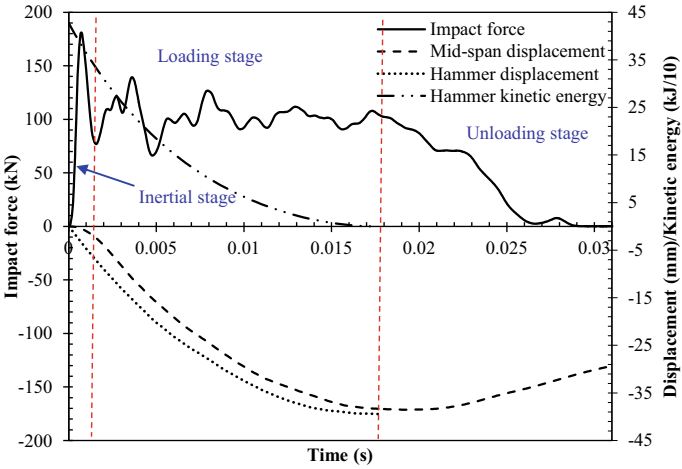

Fig. 6.7 Typical impact force, kinetic energy and displacement–time histories of SESCS beam, reprinted from Wang et al. (2021), copyright 2022, with permission from Elsevier

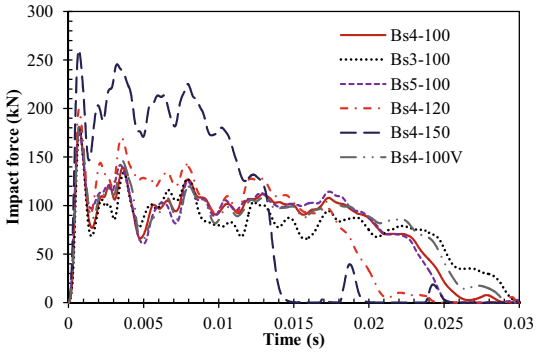

Fig. 6.8 Impact force–time histories of test specimens, reprinted from Wang et al. (2021), copyright 2022, with permission from Elsevier

from the beam. The kinetic energy of the hammer is also presented in Fig. 6.7, and it exhibits continuous decrease once the hammer strikes the beam. Moreover, the monotonic increases of the hammer and mid-span displacements are also observed. The impact energy of the hammer is completely absorbed by the SESCS sandwich beam when the hammer and mid-span displacements reach their maximum values. Moreover, the kinetic energy of the hammer also reduces to zero. It is also noted in Fig. 6.7 that the impact energy absorbed through local indentation of the beam is minimal and only occurs at inertial stage. Hence, the majority of the impact energy is dissipated via global deformation of the SESCS sandwich beam.

Figure 6.8 presents the comparison of impact force–time histories of the SESCS sandwich beams, and all the curves initially exhibit rapid increase to their peak values, followed by the post-peak stable phase and decreasing phase. The load–mid-span displacement curves of the SESCS sandwich beams are plotted in Fig. 6.9, and the

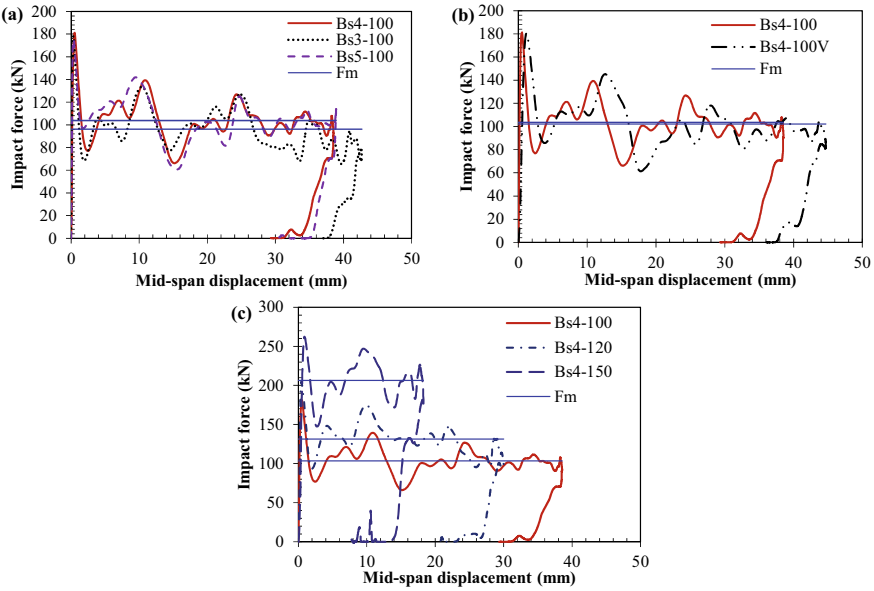

Fig. 6.9 Impact force–mid-span displacement curves of test specimens: effects of **a** faceplate thickness, **b** impact velocity and **c** concrete thickness, reprinted from Wang et al. (2021), copyright 2022, with permission from Elsevier

effects of faceplate thickness, impact velocity and concrete core thickness on the load–mid-span displacement curves can also be revealed from Fig. 6.9. Further, the post-peak mean force (F_m), which is defined in Eq. (6.1) (Wang et al. 2014), is plotted in Fig. 6.9 for comparison.

$$F_m = \frac{\int_{D_o}^{D_{mm}} F dD}{D_{mm} - D_o} \tag{6.1}$$

where D_{mm} is the maximum mid-span displacement, D_o is the mid-span displacement corresponding to first peak impact force, and F is the impact force. Figure 6.9a shows that faceplate thickness has negligible effect on the peak impact force, i.e., the differences of peak impact forces between Bs4-100, Bs3-100 and Bs5-100 are less than 3.3%, as presented in Table 6.3. The similar peak impact forces of these three specimens can be attributed to the fact that these three specimens share similar local contact stiffness, beam mass, drop weight and velocity. With regard to the post-peak mean force which can represent the resistance of the beam, it is increased by 7.8% on increasing faceplate thickness from 2.84 to 3.52 mm, and further increasing faceplate thickness to 4.46 mm has negligible effect on the post-peak mean force owing to lower strength of faceplate and larger slippage being observed for Bs5-100. Figure 6.9b presents the comparison of load–mid-span displacement curves of the

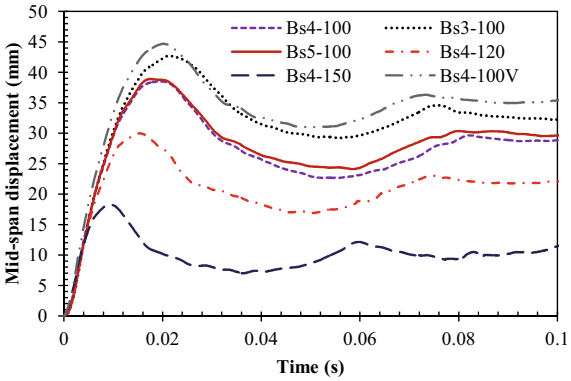

Fig. 6.10 Mid-span displacement–time histories of test specimens, reprinted from Wang et al. (2021), copyright 2022, with permission from Elsevier

SESCS sandwich beams with different drop heights, and increasing drop height from 1.2 to 1.4 m exhibits little effect on the peak impact force and post-peak mean force. The effect of concrete core thickness on the load–mid-span displacement curves of the SESCS sandwich beams is illustrated in Fig. 6.9c. The peak impact force is increased by 13.1 and 44.7%, respectively, on increasing concrete core thickness from 100 mm to 120 and 150 mm, owing to the increased beam mass and local contact stiffness. In addition, increasing concrete core thickness also results in the corresponding increase of post-peak mean force by 26.9 and 99.1%, respectively, owing to the improved resistance of the beam.

Figure 6.10 presents the mid-span displacement–time curves of the six SESCS sandwich beams. The beams exhibit continuous and rapid increase of deflection to their peak values after struck by the hammer. Subsequently, the mid-span displacements decrease when the hammer and beam start to rebound and move upwards. The following constant value of mid-span displacement (i.e., permanent displacement) can be observed. The comparison of maximum displacements of the beams is presented in Table 6.3. Generally, the maximum defection of the SESCS sandwich beam is found to decrease with the increase of faceplate thickness. The maximum mid-span displacement of the SESCS sandwich beam is decreased by 9.7% on increasing the faceplate thickness from 2.84 to 3.52 mm owing to the improved resistance of the beam, and further increasing faceplate thickness to 4.46 mm exhibits negligible influence on the maximum displacement. It is also noted in Table 6.3 that increasing concrete core thickness results in evident reduction of maximum deflection of the SESCS sandwich beam owing to the improved resistance, i.e., the maximum mid-span displacement is decreased by 22.2 and 52.6%, respectively, on increasing the concrete core thickness from 100 mm to 120 and 150 mm.

6.2.2 Numerical Study

6.2.2.1 FE Model Establishment

FE modeling of the SESCS sandwich beam under drop-weight impact loading was conducted by employing the explicit code in LS-DYNA (Hallquist 2006). Figure 6.11 presents a typical half-symmetric FE model of the SESCS sandwich beam. As the measured deformed shapes of the SESCS sandwich beams after the drop-weight impact tests were not exactly symmetrical about their mid-spans, a shift of impact point by 10 mm away from the mid-span was employed in the FE model. The concrete, support and hammer were meshed with eight-node hexahedral elements with reduced integration, and a stiffness-based hourglass control was employed for preventing zero energy modes of the hexahedral element. The top and bottom plates were meshed with Belytschko-Tsay shell elements, and five integration points were chosen along the thickness of the shell element. The stiffeners were meshed with eight-node thick-shell elements, which was convenient for the contact treatment between the stiffeners and concrete. The bolts were meshed with Hughes-Liu beam elements. The element size was determined as 10 mm based on the mesh sensitivity analysis. As illustrated in Fig. 6.12, the impact force and mid-span displacement over time curves obtained from the FE models with current element size (10 mm) and smaller element size (5 mm) are found to be well matched. Hence, the current element size was employed in the following analyses to reduce the computation time. The contacts between two parts in the FE model were simulated via employing the keyword "*Contact_Automatic_Surface_to_Surface" in LS-DYNA (Hallquist 2013). The soft constraint-based contact approach was employed for the contacts between the concrete and steel which had different material stiffness parameters. The stiffness-based contact approach was utilized to model the other contacts between two

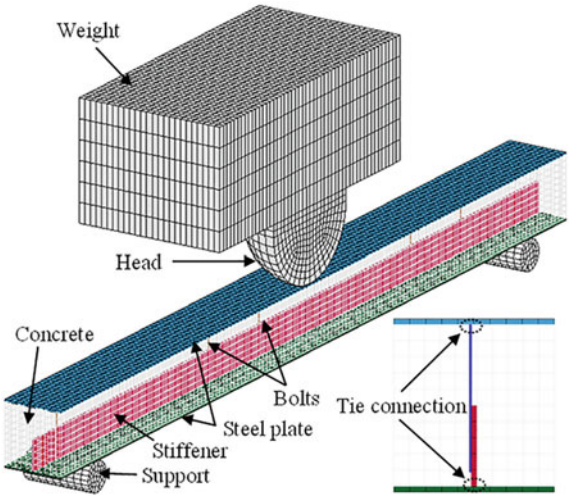

Fig. 6.11 Half-symmetric FE model of SESCS sandwich beam, reprinted from Wang et al. (2021), copyright 2022, with permission from Elsevier

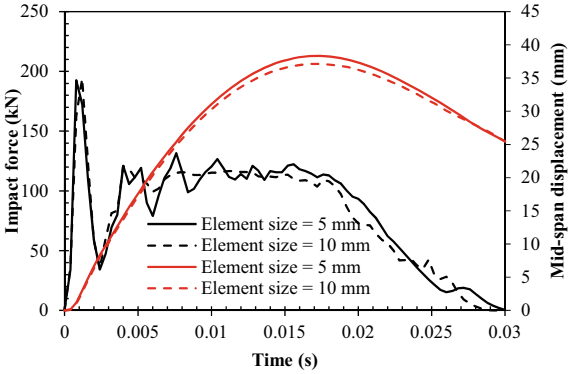

Fig. 6.12 Mesh sensitivity study of the FE model, reprinted from Wang et al. (2021), copyright 2022, with permission from Elsevier

steel parts. There was no connection failure between the bolts and top plate as well as between the stiffeners and bottom plate being observed during the test. The selected nodes of the bolts and stiffeners were tied to the top and bottom plate, respectively, via keyword "*Contact_Tied_Nodes_to_Surface", as illustrated in Fig. 6.11. The perfect bond behavior between the concrete and bolts was assumed in the FE model, and this approach has been applicable to modeling the SCS sandwich panels and reinforced concrete structures under dynamic loading (Wang et al. 2016; Li et al. 2015; Chen et al. 2015). The nodes at the bottom of the round bar supports were constrained in the translational and rotational directions. The keyword "*Initial_Velocity_Generation" in LS-DYNA was employed to specify an initial impact velocity of the drop hammer which was consistent with the measured impact velocity from the drop-weight impact test. The damping was not considered in the FE model, as it has negligible effect on the maximum displacement of the sandwich structure under impact loading (Liew et al. 2015; Yan et al. 2020a, b, c, d).

Steel material of the SESCS sandwich beam was modeled with the Piecewise Linear Plasticity model with the strain rate effect being considered via employing the Cowper-Symonds model. Figure 6.13 presents the input true stress–effective plastic

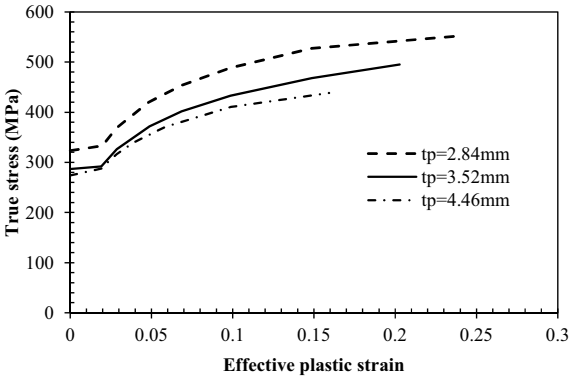

Fig. 6.13 True tress–effective strain curves for FE analyses, reprinted from Wang et al. (2021), copyright 2022, with permission from Elsevier

strain curves of the mild steels obtained from the tensile coupon tests. The flow stress of the mild steel is enhanced by multiplying a factor of $1+\left(\dot{\varepsilon}_{eff}^{p}/C\right)^{1/P}$ with the strain rate parameters C and P to be defined as 802 s^{-1} and 3.585, respectively (Abramowicz and Jones 1986). With regard to the modeling of concrete, the Continuous Surface Cap (CSC) model (FHWA 2007a, b) was employed, as it had successful application in modeling concrete material under impact and blast loading (Wang et al. 2016; Yan et al. 2020a). The failure surface, flow rule, damage formulation and strain rate effect treatment of the CSC model were presented by FHWA (2007b). This model is user-friendly, since the default parameters of the CSC model can be generated by inputting mass density and unconfined compressive strength of the concrete.

6.2.2.2 FE Results and Discussions

The comparison of failure modes of the SESCS sandwich beam (Bs4-100) obtained from the FE analysis and drop-weight impact test is presented in Fig. 6.14. The flexural failure model of the SESCS sandwich beam with plastic hinge at the mid-span can be reasonably captured by the established FE model. It can be seen from the damage contour in Fig. 6.14 that the concrete exhibits more severe damage at the mid-span and support where the cracking and crushing of concrete are observed from the test.

Figure 6.15 presents the comparison of impact force–time curves obtained from the impact tests and FE analyses, and the FE models are shown to provide accurate predictions on the impact force responses of the SESCS sandwich beams. The peak impact forces and post-peak mean forces of the SESCS sandwich beams obtained from the FE analyses are compared with those from impact tests, and the comparison is given in Table 6.4. The differences of peak impact forces between the FE-predictions and test results are found to be less than 10%, and the differences of post-peak mean forces are less than 12%. The average FE to test ratios of peak impact force and post-peak mean force are 1.07 and 1.08, respectively, and their

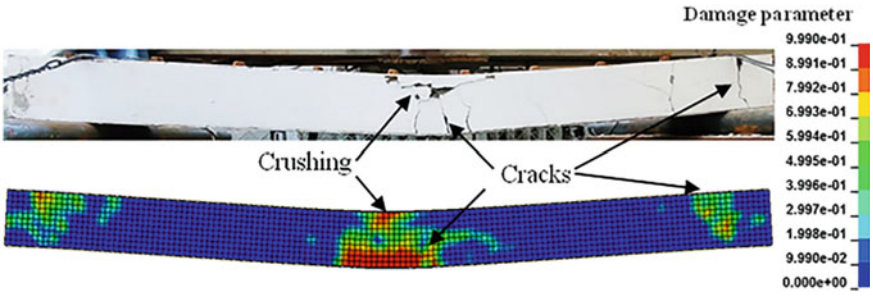

Fig. 6.14 Comparison of failure modes between FE and test, reprinted from Wang et al. (2021), copyright 2022, with permission from Elsevier

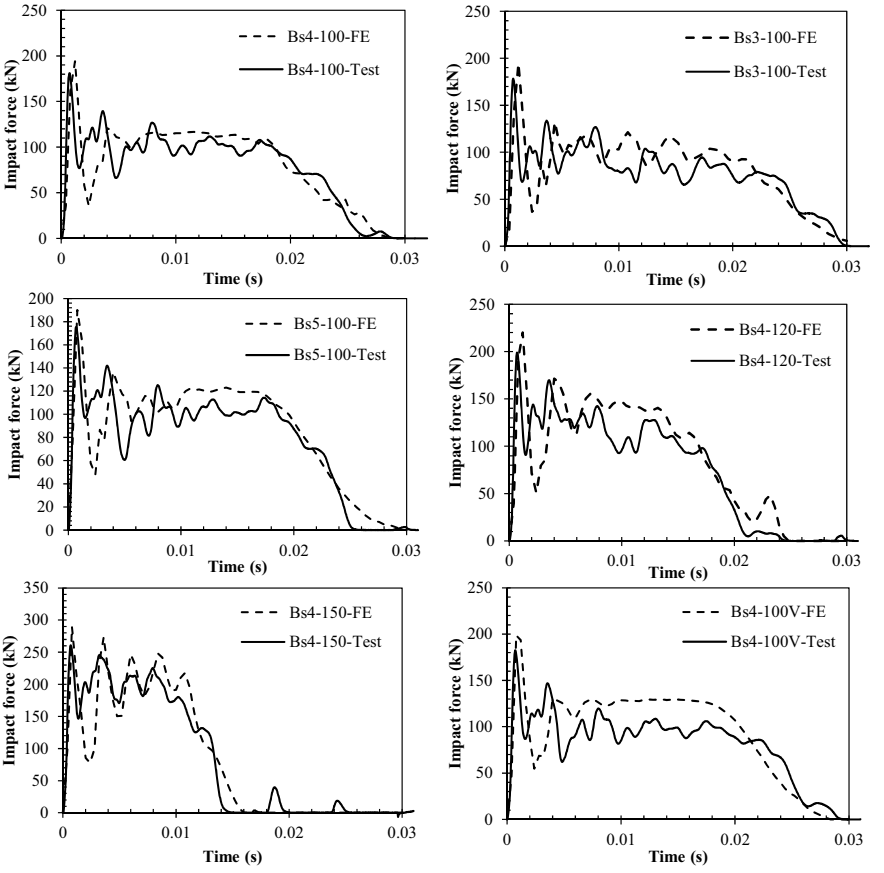

Fig. 6.15 Comparison of impact force–time histories, reprinted from Wang et al. (2021), copyright 2022, with permission from Elsevier

corresponding coefficients of variation are 0.028 and 0.056, respectively. Figure 6.16 presents the comparison of displacement responses of the SESCS sandwich beams obtained from the FE analyses and impact tests, and good agreement between them can also be observed. Table 6.4 indicates that the differences of maximum mid-span displacements of the SESCS sandwich beams obtained from the FE analyses and impact tests are within 4%, except for the specimen Bs4-150 whose maximum mid-span displacement is over-predicted by 11%. This may be attributed to the absence of adhesive bonding between the concrete and steel plates in the FE model as well as the geometric imperfection of the fabricated specimen. The average FE to test ratio of maximum mid-span displacement is 1.02 with coefficient of variation to be 0.055. The comparisons of FE-predictions and test results in terms of failure mode, impact force and displacement response can demonstrate the accurate predictions provided by the established FE models of the SESCS sandwich beams.

Table 6.4 Comparison of FE and analytical predictions with test results

Specimen	F_{maxFE} (kN)	F_{maxFE}/F_{max}	F_{mFE} (kN)	F_{mFE}/F_m	D_{mmFE} (mm)	D_{mmFE}/D_{mm}	D_{mmA} (mm)	D_{mmA}/D_{cm}
Bs4-100	194.09	1.07	113.32	1.09	37.14	0.96	40.81	1.06
Bs3-100	194.88	1.09	107.68	1.12	41.38	0.97	41.45	0.97
Bs5-100	190.00	1.08	113.04	1.09	38.54	0.99	38.56	0.99
Bs4-120	220.00	1.07	146.72	1.12	31.08	1.04	31.83	1.06
Bs4-150	289.25	1.10	198.03	0.96	20.35	1.11	22.44	1.23
Bs4-100 V	185.00	1.02	112.84	1.10	45.64	1.02	46.59	1.04
Average	–	1.07	–	1.08	–	1.02	–	1.06
COV	–	0.028	–	0.056	–	0.055	–	0.086

Note The parameters with *FE* and *A* as the subscript stand for the FE and analytical predictions, respectively

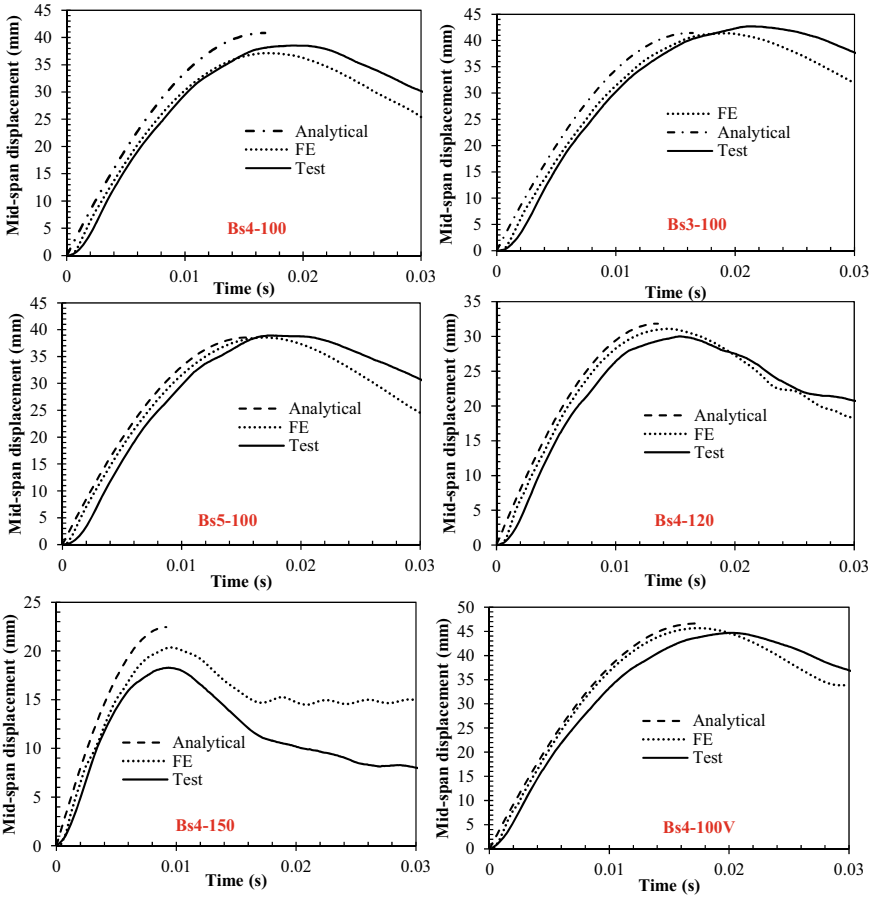

Fig. 6.16 Comparison of displacement–time histories, reprinted from Wang et al. (2021), copyright 2022, with permission from Elsevier

Figure 6.17 presents the concrete damage evolution of the specimen Bs4-100 during impact. The upper layer of the concrete at the mid-span exhibits immediate local damage once struck by the hammer (see concrete damage contour at 0.4 ms in Fig. 6.17). Subsequently, the lower part of the concrete core at the mid-span also experiences evident damage at 0.8 ms, which is caused by the tensile stress. With further impact by the hammer, the vertical cracking near the support occurs at 2.8 ms after the impact. The concrete damage contour of Bs4-100 at 17.2 ms when its maximum deflection occurs is also presented in Fig. 6.17. The severe damage of concrete is observed at the mid-span with more severe damage located at the bottom surface, which confirms the flexural failure mode of the beam.

Figure 6.18a presents the plastic strain evolutions of the top plate, stiffener and bottom plate. The top plate below the hammer immediately experiences local plastic

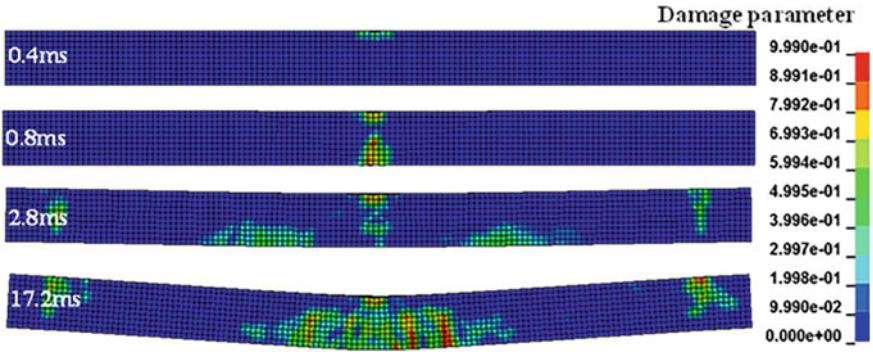

Fig. 6.17 Damage evolution of concrete of Bs4-100 during impact, reprinted from Wang et al. (2021), copyright 2022, with permission from Elsevier

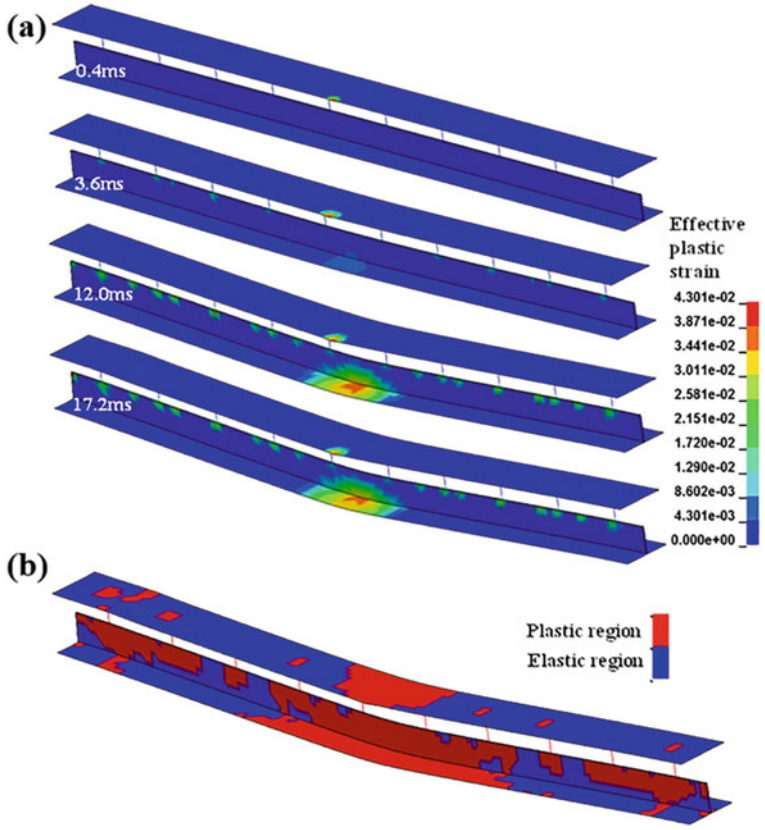

Fig. 6.18 Plastic strain distributions of steels of Bs4-100: **a** Plastic strain evolution of steel components, **b** Plastic strain distributions of steel components at 17.2 ms, reprinted from Wang et al. (2021), copyright 2022, with permission from Elsevier

deformation at 0.4 ms once the hammer strikes the beam. The local plastic deformation region of the top plate continuously grows with further impact of the hammer (see effective plastic strain contour of the top plate at 3.6 ms in Fig. 6.18a). Subsequently, the plastic deformation also occurs to the bottom plate (at the mid-span) and stiffener (at the mid-span and regions welded with bolts). The plastic deformations of the top plate, stiffener and bottom plate exhibit continuous growing with increasing deflection of the beam (i.e., larger plastic strain values and plastic deformation regions), as can be seen in Fig. 6.18a at time of 12.0 and 17.2 ms. The regions of the top plate, stiffener and bottom plate that experience plastic deformations are clearly presented in Fig. 6.18b. The whole cross-sections of the top plate, stiffener and bottom plate yield at the mid-span of the beam, which indicates the effective enhancement of the stiffener to the bending resistance of the beam. In addition, the plastic deformations of the stiffener are observed at the regions welded with bolts, which is caused by the longitudinal shear forces from the bolts. The effective bonding behavior between the stiffener and bolts plays essential roles on preventing the shear failure of bolts which was observed for the SCS sandwich beam without stiffeners after the drop-weight impact test.

6.2.3 Analytical Study

The analytical model for predicting the global displacement–time history of the SESCS sandwich beam is presented in this section. Generally, both local and global deformation of a structural member determines its impact-induced damage level (Wang et al. 2015b). Owing to the insignificant local damage of the SESCS sandwich beam observed from the drop-weight impact test, the damage level of the SESCS sandwich beam can be dominated by its global deformation. Hence, the maximum global defection of the SESCS sandwich beam can be employed for evaluating its impact-induced damage level, similar to the damage level evaluation of the structural member under blast loading (ASCE 2011). The analytical model presented in this section can be a simple alternative for predicting the damage level of the SESCS sandwich beam under impact loading.

6.2.3.1 Analytical Formulation

It is assumed that the SESCS sandwich beam immediately moves downwards with the velocity being identical to the hammer once it is struck by the hammer. Hence, an equivalent Single-Degree-of-Freedom (SDOF) system can be employed for representing the displacement response of the SESCS sandwich beam under impact loading, as illustrated in Fig. 6.19. This approach has also been successfully applied in predicting the displacement responses of the SCS sandwich beams and panels under low-velocity impact loading (Liew et al. 2009; Guo and Zhao 2019b). The equation of motion of the SDOF system can be written as

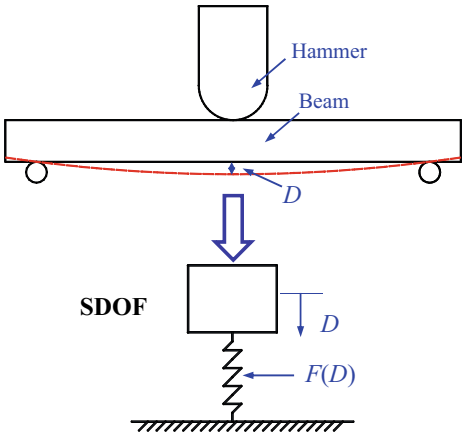

Fig. 6.19 Equivalent SDOF system for SESCS sandwich beam under impact loading, reprinted from Wang et al. (2021), copyright 2022, with permission from Elsevier

$$(m_e + m_h)\ddot{D} + F(D) = 0 \tag{6.2}$$

where m_e is the equivalent mass of the beam, m_h is the hammer mass, and $F(D)$ is the resistance versus displacement relationship of the beam. The equivalent mass of the beam can be given as

$$m_e = k_m m_b \tag{6.3}$$

where k_m and m_b are the mass factor and beam mass, respectively. The mass factor is calculated as (Biggs 1964)

$$k_m = \frac{\int_0^L \varphi^2(x)dx}{L} \tag{6.4}$$

where L is the clear span of the beam, and $\varphi(x)$ is the shape function and given in Eq. (6.5) for the left half-span ($x < L/2$) (Biggs 1964).

$$\varphi(x) = \begin{cases} \frac{x}{L^3}\left(3L^2 - 4x^2\right) & \text{elastic} \\ \frac{2x}{L} & \text{plastic} \end{cases} \tag{6.5}$$

With regard to the resistance–displacement function of the beam under concentrated load at the mid-span, $F(D)$, the flexural resistance and deflection are calculated, since they govern the resistance and deflection of the beam with flexural failure mode. The following assumptions are employed for simplifying the calculation of yielding and ultimate bending moment of the SESCS sandwich beam: (a) the steel faceplates abide by the elastic-perfectly plastic behavior, (b) plane section assumption still works in the SESCS sandwich beam and (c) tension strength of concrete is negligible. In the

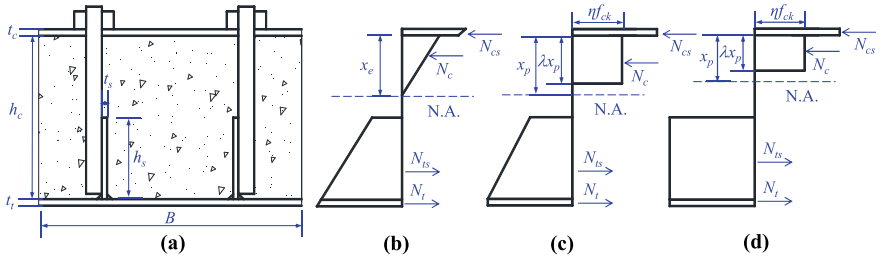

Fig. 6.20 Stress diagram for bending resistance calculation of SESCS sandwich beam: **a** cross-section, **b** stress for yielding bending resistance **c** stress for ultimate bending resistance (yielding of partial cross-section of stiffener) and **d** stress for ultimate bending resistance (yielding of whole cross-section of stiffener), reprinted from Wang et al. (2021), copyright 2022, with permission from Elsevier

elastic range, both the strain and stress are linearly distributed along the depth of the SESCS sandwich beam, as illustrated in Fig. 6.20. Employing the force equilibrium gives

$$N_t + N_{ts} - N_c - N_{cs} = 0 \tag{6.6}$$

Based on the linear relationship of stress and strain in the elastic range, the resultant forces in Eq. (6.6) can be obtained as

$$\begin{aligned}
N_t &= \frac{h_c - x_e + t_t/2}{x_e} E_s \varepsilon_e t_t B \\
N_{ts} &= \frac{2h_c - 2x_e - h_s}{x_e} E_s \varepsilon_e h_s t_s \\
N_c &= \frac{1}{2} x_e B E_c \varepsilon_e \\
N_{cs} &= \min\left(\frac{x_e + t_c/2}{x_e} E_s \varepsilon_e t_c B, n P_{Rd} \right) \\
P_{Rd} &= \min\left(0.2 f_u \pi d^2/\gamma_v, 0.29 \alpha d^2 \sqrt{f_{ck} E_c}/\gamma_v \right)
\end{aligned} \tag{6.7}$$

As illustrated in Fig. 6.20, N_t, N_{ts}, N_c, N_{cs} are the resultant forces of the bottom plate, stiffener, concrete and top plate, respectively; x_e denotes the neutral axis position; h_c, t_t, h_s, t_c and B are the geometric parameters of the SESCS sandwich beam in Fig. 6.20; E_s and E_c are the Young's modulus of steel and concrete, respectively; ε_e is the strain at the top compression fiber of the concrete corresponding to the end of elastic range; P_{Rd}, n and d are the shear strength of single bolt connector as specified in Eurocode 4 (2004a), number of bolt connectors provided between maximum moment and zero moment, and diameter of bolt connector, respectively;

f_u and f_{ck} are the ultimate strength of bolt connector and compressive strength of concrete; γ_v is the partial factor (Eurocode 2004b).

If $N_{cs} = \frac{x_e + t_c/2}{x_e} E_s \varepsilon_e t_c B$, substituting Eqs. (6.7) into (6.6) leads to the neutral axis position, x_e, as

$$x_e = \frac{-I_1 + \sqrt{I_1^2 + 2BKI_2}}{BK} \tag{6.8}$$

where $K = E_c/E_s$, $I_1 = (t_t + t_c)B + 2h_s t_s$, $I_2 = \left(t_t h_c + t_t^2/2 - t_c^2/2\right)B + (2h_c - h_s)h_s t_s$. If $N_{cs} = nP_{Rd}$, the neutral axis position, x_e, is calculated as

$$x_e = \frac{-I_3 + \sqrt{I_3^2 + 2BKI_4}}{BK} \tag{6.9}$$

where $I_3 = t_t B + 2h_s t_s + nP_{Rd}/E_s\varepsilon_e$, $I_4 = t_t B(h_c + t_t/2) + (2h_c - h_s)h_s t_s$. The yielding bending moment, M_y, can be obtained by taking moment about the acting point of N_{cs} as

$$\begin{aligned} M_y = {} & \frac{\varepsilon_e(h_c - x_e + t_t/2)}{xe} E_s B t_t (h_c + t_t/2 + t_c/2) \\ & + \frac{2\varepsilon_e(h_c - x_e - h_s)}{x_e} E_s h_s t_s (h_c - h_s/2 + t_c/2) \\ & + \frac{\varepsilon_e(h_c - x_e)}{x_e} E_s h_s t_s (h_c - h_s/3 + t_c/2) - \frac{1}{2}\varepsilon_e E_c x_e B(x_e/3 + t_c/2) \end{aligned} \tag{6.10}$$

where $\varepsilon_e = \min(\varepsilon_1, \varepsilon_2, \varepsilon_3)$. ε_1, ε_2 and ε_3 are the strains at the top compression fiber of the concrete corresponding to three cases of the end of elastic range, and they are given as follows:

Case 1: the yielding of bottom plate, i.e., $\sigma_t = f_y$, which leads to

$$\varepsilon_1 = \frac{x_e f_y}{(h_c - x_e + t_t)E_s} \tag{6.11}$$

Case 2: the strain of concrete reaches the limit of elastic strain, i.e., $\sigma_c = 0.4 f_{cu}$ (Eurocode 2004b), which gives

$$\varepsilon_2 = \frac{0.4 f_{cu}}{E_c} \tag{6.12}$$

Case 3: the shear strength of bolt connector is reached and $Ncs = nPRd$, we have

$$\varepsilon_3 = \frac{nP_{Rd}}{Bt_c E_s} \tag{6.13}$$

With regard to the ultimate bending moment calculation for the SESCS sandwich beam, the force equilibrium in Eq. (6.6) is also applied, and the resultant forces can be given as

$$\begin{aligned} N_t &= f_y B t_t \\ N_{cs} &= \min\left(f_y B t_c, nP_{Rd}\right) \\ N_c &= \lambda x_p \eta f_{ck} B \end{aligned} \tag{6.14}$$

where λ and η are the factors defining the effective height of compression zone and effective strength of concrete, respectively. They are given as (Eurocode 2004b)

$$\begin{aligned} \lambda &= \begin{cases} 0.8 & f_{ck} \le 50\text{MPa} \\ 0.8 - (f_{ck} - 50)/400 & 50\text{MPa} \le f_{ck} \le 90\text{MPa} \end{cases} \\ \eta &= \begin{cases} 1.0 & f_{ck} \le 50\text{MPa} \\ 1.0 - (f_{ck} - 50)/200 & 50\text{MPa} \le f_{ck} \le 90\text{MPa} \end{cases} \end{aligned} \tag{6.15}$$

The ultimate bending moment of the SESCS sandwich beam is reached when the top compression fiber of the concrete reaches ultimate compressive strain, ε_{cu}. They are two different stress distributions of the stiffeners when the ultimate bending moment is achieved, i.e., partial or whole cross-section of the stiffener yields, as illustrated in Figs. 6.20c, d, respectively. When the strain at the top layer of the stiffener exceeds yield strain, ε_{sy}, whole cross-section of the stiffener yields, which leads to

$$\frac{h_c - x_p - h_s}{x_p}\varepsilon_{cu} \ge \varepsilon_{sy} \tag{6.16}$$

Then, we have

$$x_p \le \frac{\varepsilon_{cu}(h_c - h_s)}{\varepsilon_{cu} + \varepsilon_{sy}} \tag{6.17}$$

In this case, the resultant force of the stiffener, N_{ts}, is given as

$$N_{ts} = 2h_s t_s f_y \tag{6.18}$$

Substituting Eqs. (6.14) and (6.18) into Eq. (6.6) yields

$$N_{cs} + \lambda \eta x_p B f_c - 2h_s t_s f_y - B t_t f_y = 0 \tag{6.19}$$

Then, we have

$$x_p = \frac{2h_s t_s f_y + Bt_t f_y - N_{cs}}{\lambda \eta B f_c} \tag{6.20}$$

Hence, if $\frac{2h_s t_s f_y + Bt_t f_y - N_{cs}}{\lambda \eta B f_c} \leq \frac{\varepsilon_{cu}(h_c - h_s)}{\varepsilon_{cu} + \varepsilon_{sy}}$, the whole cross-section of the stiffener yields, and Eqs. (6.19) and (6.20) are applicable. Taking moment about the acting point of N_c gives the ultimate bending moment of the SESCS sandwich beam as

$$M_u = f_y B t_t \left(\frac{2h_c + t_t - \lambda x_p}{2} \right) + N_{cs} \left(\frac{t_c + \lambda x_p}{2} \right) + f_y t_s h_s \left(2h_c - \lambda x_p - h_s \right) \tag{6.21}$$

If $\frac{2h_s t_s f_y + Bt_t f_y - N_{cs}}{\lambda \eta B f_c} > \frac{\varepsilon_{cu}(h_c - h_s)}{\varepsilon_{cu} + \varepsilon_{sy}}$, the partial cross-section of the stiffener yields. The force equilibrium gives

$$N_{cs} + \lambda \eta x_p B f_c - 2t_s \left\{ h_s f_y - \frac{\left[f_y - \frac{h_c - x_p - h_s}{x_p} \varepsilon_{cu} E_s \right] \left[h_s - h_c + \frac{(\varepsilon_{cu} + \varepsilon_{sy}) x_p}{\varepsilon_{cu}} \right]}{2} \right\} - Bt_t f_y = 0 \tag{6.22}$$

Then, x_p can be calculated as

$$x_p = \frac{-I_5 + \sqrt{I_5^2 + 4 I_6 I_7}}{I_6 t_s} \tag{6.23}$$

where $I_5 = (h_s - h_c)\left(f_y - \varepsilon_{cu} E_s + \left(\varepsilon_{cu} + \varepsilon_{sy} \right) / \varepsilon_{cu} \right)$, $I_6 = \left(f_y - \varepsilon_{cu} E_s \right) \left(\varepsilon_{cu} + \varepsilon_{sy} \right) / \varepsilon_{cu} t_s$, $I_7 = t_s (h_s - h_c)^2 - 2h_s t_s f_y - B f_y t_t + N_{cs}$. Then, the ultimate bending moment of the SESCS sandwich beam can be given in Eq. (6.24) by taking moment about the acting point of N_c.

$$\begin{aligned} M_u = {} & f_y B t_t \left(h_c + t_t/2 - \lambda x_p/2 \right) + N_{cs} \left(t_c/2 + \lambda x_p/2 \right) + 2 f_y t_s h_s \left(h_c - \lambda x_p/2 - h_s/2 \right) \\ & - t_s \left(f_y - \frac{h_c - x - h_s}{x} \varepsilon_{cu} E_s \right) \left[h_s - h_c + \frac{(\varepsilon_{cu} + \varepsilon_{sy}) x p}{\varepsilon_{cu}} \right] \\ & \left[h_c - x_p/2 - h_s + h_c/3 - \frac{(\varepsilon_{cu} + \varepsilon_{sy}) x_p}{3 \varepsilon_{cu}} \right] \end{aligned} \tag{6.24}$$

The curvatures corresponding to the yielding and ultimate bending moment of the SESCS sandwich beam (ϕ_y and ϕ_p) can be given as

$$\phi_y = \frac{\varepsilon_e}{x_e}; \quad \phi_p = \frac{\varepsilon_{cu}}{x_p} \tag{6.25}$$

Then, the corresponding mid-span displacements can be calculated as

$$D_y = \frac{\phi_e L^2}{12}; \quad D_u = \frac{\phi_p L^2}{12} \tag{6.26}$$

Herein, the calculation of D_u is based on the "minimum stiffness principle" (Gu et al. 2015), which assumes that the bending stiffness along the whole span of the beam is the same, and the bending stiffness at the position with maximum bending moment (or minimum bending stiffness) is chosen for the deflection calculation. This method leads to larger curvature and flexure-induced deflection of the beam as compared to the actual one. However, the shear deformation of the beam which is not considered in this method may offset the calculation deviance due to using the "minimum stiffness principle". The resistances of the beam corresponding to the yielding and ultimate bending moment (F_y and F_u) are given as

$$F_y = \frac{4M_y}{L}; \quad F_u = \frac{4M_u}{L} \tag{6.27}$$

The tri-linear curve is employed herein to describe the resistance–displacement relationship of the SESCS sandwich beam under concentrated load at the mid-span, as illustrated in Fig. 6.21. It is known that the mild steel exhibits evident strain rate effect, and its strength increases with the increase of strain rate. The Dynamic Increase Factor (DIF) is usually employed to represent the strength enhancement. Owing to the variation of strain rate during impact, the strength enhancement or DIF also varies. The average strain rate was employed herein to simplify the treatment of strain rate effect on the strength enhancement. The maximum strain rate of the beam occurs at initial impact stage when the beam exhibits maximum velocity. Subsequently, the strain rate of the top and bottom plate at initial impact stage can be calculated in Eq. (6.28) by assuming the neutral axis is located at middle layer of the beam.

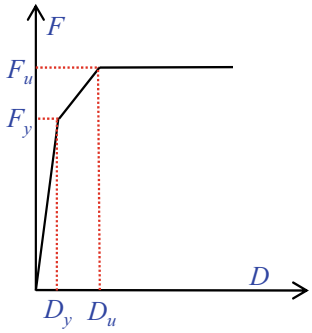

Fig. 6.21 Tri-linear force–displacement curve employed for analytical model, reprinted from Wang et al. (2021), copyright 2022, with permission from Elsevier

$$\dot{\varepsilon}_s = \left(\frac{h_c + t_c}{2}\right)\dot{\phi} \tag{6.28}$$

where $\dot{\phi}$ is the curvature rate of the beam at the mid-span and given in Eq. (6.29) by employing the elastic deflection shape function in Eq. (6.5).

$$\dot{\phi} = \frac{12V_0}{L^2} \tag{6.29}$$

where V_0 is the initial velocity of the beam and can be obtained in Eq. (6.30) by applying the conservation of momentum.

$$V_0 = \frac{m_h V}{m_e + m_h} \tag{6.30}$$

where V is the impact velocity of the hammer. Since the strain rate drops to zero when the maximum displacement is reached, the average strain rate can be taken as the half of the maximum strain rate as

$$\dot{\varepsilon}_{\bar{s}} = \dot{\varepsilon}_s/2 \tag{6.31}$$

Then, DIF of the faceplate can be obtained by employing the Cowper-Symonds model as

$$DIF_s = 1 + (\dot{\varepsilon}_{\bar{s}}/C)^{1/P} \tag{6.32}$$

To include the strain rate effect of mild steel into the analytical model, yield stress of the faceplate, f_y, in the equations for calculating the resistances is enhanced via multiplying a factor of DIF_s in Eq. (6.32). For the established SDOF system with the equation of motion being presented in Eq. (6.2), the initial displacement and velocity are zero and V_0, respectively. The numerical method can be employed to solve the equation of motion in Eq. (6.2) and obtain the displacement–time response of the SESCS sandwich beam. Herein, the fourth-order Runge–Kutta time stepping procedure was employed.

6.2.3.2 Analytical Validation

Figure 6.16 presents the comparison of mid-span displacement–time histories of the SESCS sandwich beams obtained from the analytical models with those obtained from the tests and FE analyses, and reasonable agreements among them can be observed. Table 6.4 lists the maximum mid-span displacements and their comparisons with test data. The differences of the maximum mid-span displacements

between the analytical predictions and tests are less than 6%, except for the specimen Bs4-150 with analytical-predicted maximum mid-span displacement being 23% larger than test data. The over-predicted displacement response of the specimen Bs4-150 from the analytical model may be caused by the underestimation of the stiffness of the beam after yielding due to using the "minimum stiffness principle" (Gu et al. 2015). The underestimation of the stiffness of the beam has more significant effect on the displacement response of the beam with smaller deformation. Hence, the bigger difference of the maximum mid-span displacement between the test and analytical-prediction is observed for the specimen Bs4-150 with smallest maximum mid-span displacement (18.27 mm). The average analytical-prediction to test ratio of the maximum mid-span displacement is 1.06 with coefficient of variation to be 0.086. The aforementioned comparisons demonstrate that the proposed analytical model is reasonable and can be employed as a simple alternative to predict displacement response of the SESCS sandwich beam under impact loading.

6.3 SESCS Sandwich Panel Under Impact

6.3.1 Experimental Study

6.3.1.1 Specimens

Figure 6.22 presents the SESCS sandwich panel designed for the drop-weight impact test. The fabrication process of the SESCS sandwich panel is similar to that of

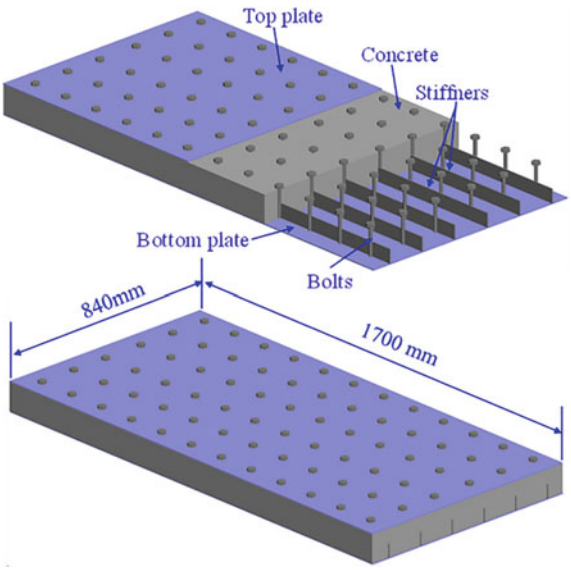

Fig. 6.22 General illustration of the SESCS sandwich panel, reprinted from Wang et al. (2022), copyright 2022, with permission from Elsevier

Table 6.5 Summary of specimens for SESCS sandwich panel (unit: mm)

Specimen	t_c	h_c	t_t	H
Ps4-70	3.52	70	3.52	1800
Ps3-70	2.84	70	2.84	1800
Ps5-70	4.46	70	4.46	1800
Ps4-80	3.52	80	3.52	1800
Ps4-90	3.52	90	3.52	1800
Pb4-70	3.52	70	3.52	1800
Ps4-70 V	3.52	70	3.52	1400

Note t_c, h_c, and t_t–Thicknesses of top plate, concrete core and bottom plate; H–Drop height; Ps and Pb stand for the SESCS sandwich panel and SCS sandwich panel, respectively

SESCS sandwich beam, which includes four steps, as illustrated in Fig. 6.2. Seven specimens were prepared for the drop-weight impact tests to study the effects of various parameters on the impact responses of SESCS sandwich panels. Table 6.5 presents the varying parameters for all the specimens. One specimen (Ps4-70) was designed as a control specimen with 3.52 mm thick steel plates and 70 mm thick concrete core. To study the effects of the steel plate and concrete core thicknesses, two specimens were designed with 2.84 and 4.46 mm thick steel plates, and two specimens were designed with concrete core thickness of 80 and 90 mm. Furthermore, one specimen with all the parameters same as the control specimen was prepared to study the influence of drop height, and one specimen was designed as a traditional SCS sandwich panel without stiffeners to compare the impact resistance with the newly developed SESCS sandwich panel. The length and width of all the specimens were same (i.e., 1700 and 840 mm for length and width, respectively). The diameter and spacing of bolts for all the specimens were 12 and 140 mm, respectively. The stiffeners of SESCS sandwich panels had the same dimension of $1700 \times 40 \times 3.52$ mm^3, and the spacing of stiffeners in width direction was 140 mm. Q235 mild steel was employed for the steel plates of the SESCS sandwich panels, and normal weight concrete was employed for the concrete core. Their material properties were obtained from the tensile coupon tests and uniaxial unconfined compressive tests for steel and concrete, respectively. Table 6.2 presents the material properties of mild steel plates, bolts and concrete.

6.3.1.2 Test Setup and Instrumentation

The drop-weight impact test method has been widely adopted by researchers to evaluate the impact resistance of the SCS sandwich structures (Lu et al. 2021; Zhao et al. 2018). Hence, in this study, the impact tests on SESCS sandwich panels were performed using a drop-weight impact test system, as shown in Fig. 6.23 for the impact test setup and instrumentation. The preliminary FE simulations on the SESCS sandwich panels were conducted to obtain the suitable mass and drop height of the

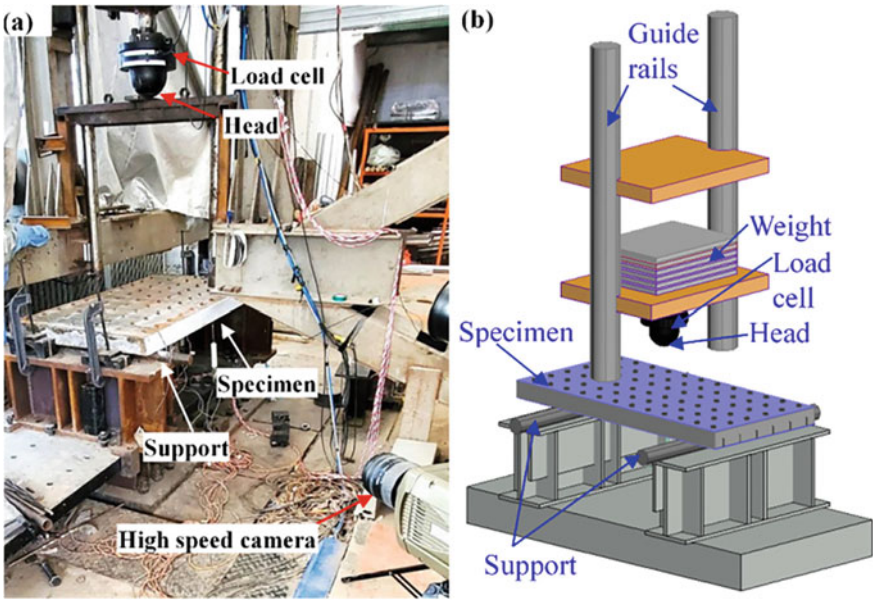

Fig. 6.23 Test setup and instrumentation: **a** Photograph and **b** schematic view, reprinted from Wang et al. (2022), copyright 2022, with permission from Elsevier

hammer. The mass of the hammer for all the specimens was 590 kg, and the hammer was dropped freely from the height of 1.8 m for all the specimens except for one specimen which was subjected to a drop height of 1.4 m (refer to Table 6.5). The SESCS sandwich panels were simply supported on two circular bar supports with a clear span of 1500 mm, as presented in Fig. 6.23. It should be mentioned that the specimens were tied to the support using steel wires to prevent the uplift of the specimens during their rebounds. A dynamic load cell was embedded in the hammer head to measure the impact force, and three potentiometers (one at the center of the panel, one at the free side of the panel in mid-span, and one at quarter-span) were used to measure the displacements of the specimens. A data logger with a sampling frequency of 100 kHz was employed for recording the impact force–and displacement–time histories. The impact process and deformation of the SESCS sandwich panels were captured using a high-speed camera with a sampling frequency of 3000 frames/sec.

6.3.1.3 Test Results and Discussions

There were seven specimens subjected to impact load at their centers using the hemispherical drop hammer. The test results are summarized in Table 6.6, including peak impact forces and maximum displacements recorded by the dynamic load cell and three potentiometers, respectively.

Table 6.6 Summary of test results for SESCS sandwich panel

Specimen	F_{max} (kN)	F_m (kN)	D_{mm} (mm)	D_{mms} (mm)	D_{qm} (mm)
Ps4-70	323.91	243.92	40.87	35.95	21.48
Ps3-70	306.35	217.70	42.26	37.10	22.60
Ps5-70	387.82	274.89	36.43	29.70	17.26
Ps4-80	371.90	270.44	33.63	28.20	17.56
Ps4-90	438.52	300.91	28.85	24.59	15.96
Pb4-70	228.81	185.20	54.03	37.04	27.97
Ps4-70 V	330.86	242.64	31.15	27.02	17.05

Note F_{max}, F_m–Peak impact force and post-peak mean force; D_{mm}, D_{mms}, D_{qm}–Maximum values of the displacements at mid-spans (center and free side) and quarter-spans of the panels

Damage Analysis of SESCS Sandwich Panels

Figure 6.24 presents the seven specimens after drop-weight impact tests, and all of them exhibit global flexural deformation mode with plastic hinges being observed at their mid-spans. The flexural deformation mode also results in vertical cracks occurred at the mid-spans of specimens, and the vertical crack width exhibits the largest value near the bottom surface and gradually decrease as the crack approaches the neutral axis. Besides the flexure-induced vertical cracks at the mid-span, the shear force-induced diagonal cracks near the support are observed for the specimens

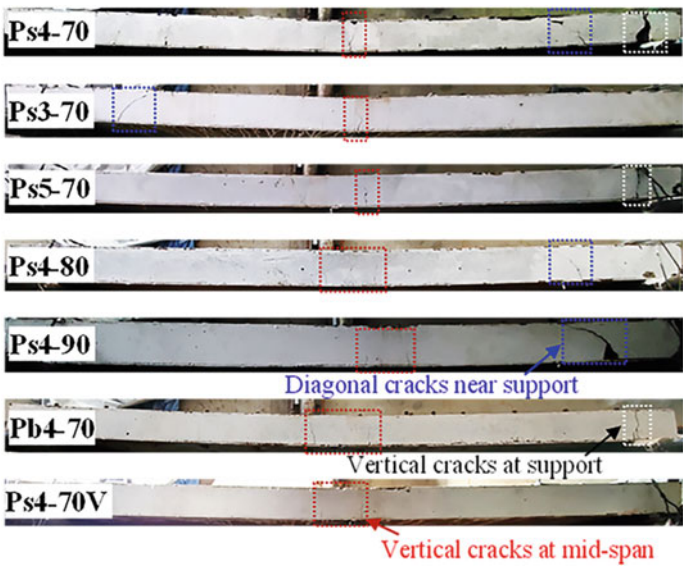

Fig. 6.24 Failure modes of SESCS sandwich panels, reprinted from Wang et al. (2022), copyright 2022, with permission from Elsevier

Ps3-70, Ps4-70, Ps4-80, and Ps4-90. Moreover, some of the specimens (Ps4-70, Ps5-70, and Ps4-70) exhibit vertical cracks of concrete above the support, which is caused by the larger reaction force. There is no fracture, buckling, or separation of the steel plates being observed for any of the tested specimens, which indicates that the structural integrity of the SESCS sandwich panels is maintained. Moreover, no slip between the concrete core and steel plates is observed, which reveals that the proposed SESCS sandwich panels exhibit desirable resistance to interfacial shear.

The comparison of cracking patterns of the specimens with variant steel plate thicknesses reveals that increasing steel plate thickness tends to reduce the occurrence of diagonal crack near the support, i.e., the diagonal crack is not observed for the specimen Ps5-70 with the thickest steel plate, while both the specimens Ps3-70 and Ps4-70 exhibit diagonal cracks. However, increasing steel plate thickness of the SESCS sandwich panel can result in the increased possibility of occurrence of vertical crack above the support, i.e., the specimens Ps4-70 and Ps5-70 with higher steel plate thickness exhibit vertical crack above the support. This is because increasing steel plate thickness leads to larger bending resistance of the SESCS sandwich panel, and thus larger reaction force from the support. It is also noted in Fig. 6.24 that increasing concrete thickness results in reduced width and length of vertical cracks at mid-span owing to the decreased impact-induced deformation of the SESCS sandwich panel. Moreover, the possibility of occurrence of vertical crack above the support is found to be reduced by increasing the thickness of concrete core, which can be attributed to the improved local bearing resistance for the panel with a thicker concrete core. The presence of stiffeners in tension plate is found to reduce the vertical crack width owing to the smaller deformation of the specimen Ps4-70 as compared to Pb4-70 without stiffeners. The drop height also exhibits a noticeable influence on the cracking patterns of the SESCS sandwich panel. Only vertical crack of concrete at mid-span is observed for the specimen Ps4-70 V with a lower drop height of 1.4 m. However, increasing drop height from 1.4 to 1.8 m causes the increase of vertical crack width at mid-span as well as the occurrence of diagonal crack near the support and vertical crack above the support.

Impact Force Response

The impact force and displacement over time responses of all the tested specimens exhibit similar behavior. Figure 6.25 presents the typical impact force–time curve as well as center and hammer displacement versus time curves to reveal the impact response of the SESCS sandwich panel. Three impact response stages can be identified based on Fig. 6.25, including inertial, loading, and unloading stages, similar to the observations by other researchers (Yan et al. 2020a, b, c, d; Zhao and Guo 2018). In the inertial stage, there is a sudden increase in the impact force within 2 ms, which is due to the inertial effect. During this stage, a contact is developed between the drop hammer and panel, initiating local indentation on the top surface. Meanwhile, the local indentation zone of the panel is forced to move downwards with the same velocity as that of drop hammer. The hammer displacement exhibits

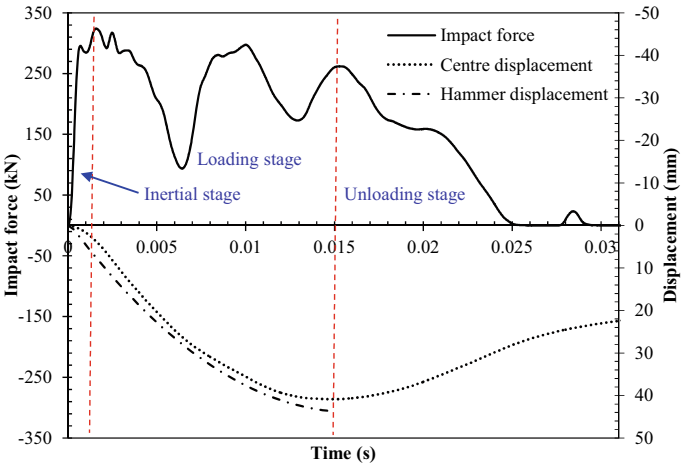

Fig. 6.25 Typical impact force and displacement–time histories of the SESCS sandwich panel, reprinted from Wang et al. (2022), copyright 2022, with permission from Elsevier

faster increase as compared to center displacement, and the displacement difference between the two increases in the inertial stage and approaches a constant value at the end of inertial stage. The loading stage occurs from 2 to 15 ms, during which the drop hammer and panel move downwards together. The impact force exhibits evident fluctuation in the loading stage, which can be attributed to the relative motion of the drop hammer and panel. With regard to center and hammer displacements in the loading stage, both of them exhibit continuous increase up to their maximum values, and the displacement difference is nearly constant. At the end of loading stage, the maximum deformation of the panel occurs, and the hammer velocity reduces to zero. The unloading stage is observed from 15 to 25 ms with the rebound of the panel. The impact force and displacement exhibit monotonic decrease in the unloading stage. The impact force drops to zero when the hammer is completely separated from the panel. Partial impact energy stored in the panel transforms to kinetic energy owing to elastic recovery of the panel.

Figure 6.26 shows the impact force–time histories of all the tested specimens, and the peak impact forces are also listed in Table 6.6. The effect of steel plate thickness on the impact force response is illustrated in Fig. 6.26a, and higher impact force in loading stage is observed for the SESCS sandwich panel with thicker steel plate owing to the improved resistance of the panel. This effect was also observed in a study conducted by Zhao et al. (2018). With regard to the peak impact force presented in Table 6.6, it also exhibits increase with the rise in steel plate thickness owing to the enhanced contact stiffness and resistance of the panel. The peak impact force is increased from 306.35 kN to 323.91 and 387.82 kN (by 5.73% and 26.59%), respectively, on increasing the thickness of steel plate from 2.84 mm to 3.52 and 4.46 mm. There is a noticeable improvement in the impact resistance of the SESCS sandwich panel with the increase of concrete core thickness, as presented in Fig. 6.26b

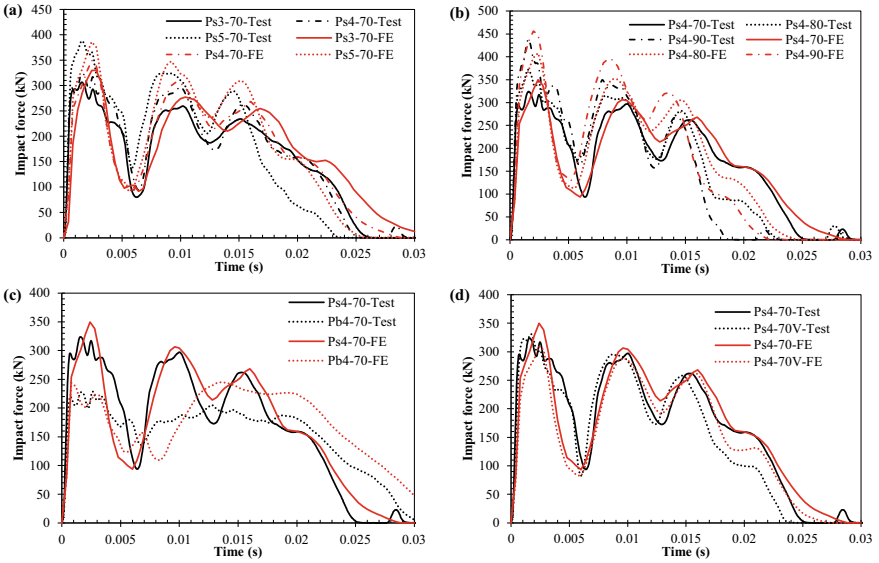

Fig. 6.26 Impact force–time histories of test specimens: effects of **a** steel plate thickness, **b** concrete core thickness, **c** presence of stiffener, and **d** drop height, reprinted from Wang et al. (2022), copyright 2022, with permission from Elsevier

and Table 6.6. The peak impact force of the SESCS sandwich panel with a 70 mm thick concrete core (Ps4-70) is 323.91 kN which is increased to 371.90 kN and 438.52 kN (by 14.81 and 35.38%), respectively, when concrete core thickness is raised to 80 and 90 mm. The increase in concrete core thickness can improve contact stiffness and resistance of the panels, which results in higher peak impact force, as demonstrated in Fig. 6.23b. Sohel and Liew (2014) also revealed that the concrete thickness influenced the impact resistance of the SCS sandwich panel. A comparison of impact force–time histories of specimens Ps4-70 and Pb4-70 are presented in Fig. 6.26c to reveal the effect of stiffeners on the impact force response of the panels. Specimen Ps4-70 is the proposed SESCS sandwich panel, whereas specimen Pb4-70 is the traditional SCS sandwich panel without stiffeners. Figure 6.26c shows that the peak impact force of the panel is increased by 41.56% on employing stiffeners in the tension plate. This demonstrates that the impact resistance of the sandwich panel is significantly improved with the presence of stiffeners. Figure 6.26d presents the effect of drop height on the impact force response of the SESCS sandwich panels, and the reduction in drop height from 1.8 m to 1.4 m exhibits negligible effect on the peak impact force (330.86 kN and 323.91 kN). However, there is a reduction in damage and deformation of the panel owing to less applied impact energy. Zhao et al. (2018) noted that there was a limited influence on the maximum impact force in the loading stage for the SCS sandwich panel subjected to different impact velocities, and this study presented the similar observation.

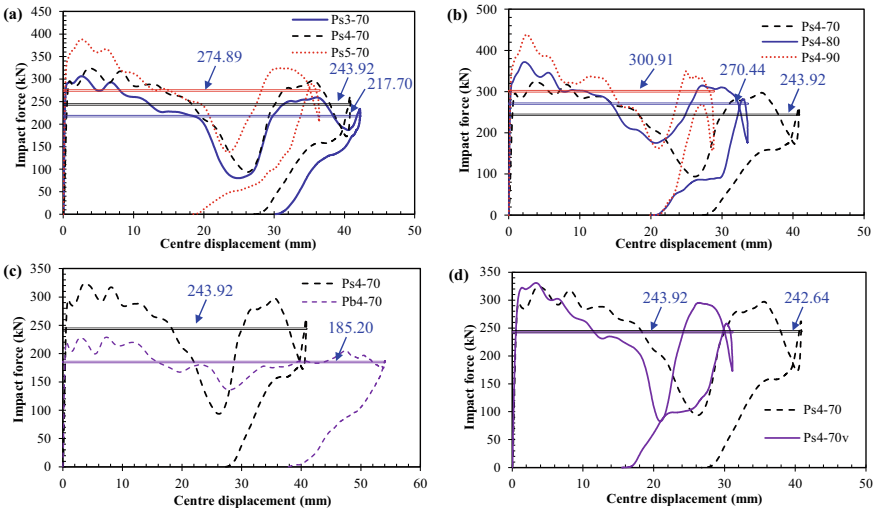

Fig. 6.27 Impact force–center displacement curve of test specimens: effects of **a** steel plate thickness, **b** concrete core thickness, **c** presence of stiffener, and **d** drop height, reprinted from Wang et al. (2022), copyright 2022, with permission from Elsevier

The peak impact force at the inertial stage cannot represent the actual resistance of the specimen because it is mainly caused by the inertial effect and strongly depends on the contact stiffness of the specimen. Nevertheless, the post-peak mean force (defined in Eq. (6.1)) could provide a better evaluation of the actual resistance of the specimen subjected to impact loading. The impact force versus center displacement curves for all the tested specimens are plotted in Fig. 6.27. There is a sharp rise in the impact force upon the impact by the hammer due to inertial effect and large contact stiffness, whereas the displacement remains below 2 mm. However, after the development of contact between the hammer and panel, the hammer forces the panel to move downwards, showing continuous increase in the displacement of the panel. Though there is continuous increase in the displacement, there are some fluctuations and drop in the impact force owing to the impact-induced vibration and crushing of the concrete at the impact point, respectively. It can be noticed from Figs. 6.27a, b that the post-peak mean force of the SESCS sandwich panel is evidently increased with the increase in the thickness of concrete core and steel plates, i.e., the post-peak mean force is increased by 23.4 and 26.3%, respectively, on increasing the concrete core thickness from 70 to 90 mm and steel plate thickness from 2.84 to 4.46 mm. The significant improved post-peak mean force (by 31.7%) of the SESCS sandwich panel can be observed in Fig. 6.27c as compared to the traditional SCS sandwich panel without stiffeners, which indicates the improved impact resistance of the SESCS sandwich panel owing to the presence of stiffeners in the tension plate. Figure 6.27d indicates that the impact velocity has negligible effect on the post-peak mean force and resistance of the specimen.

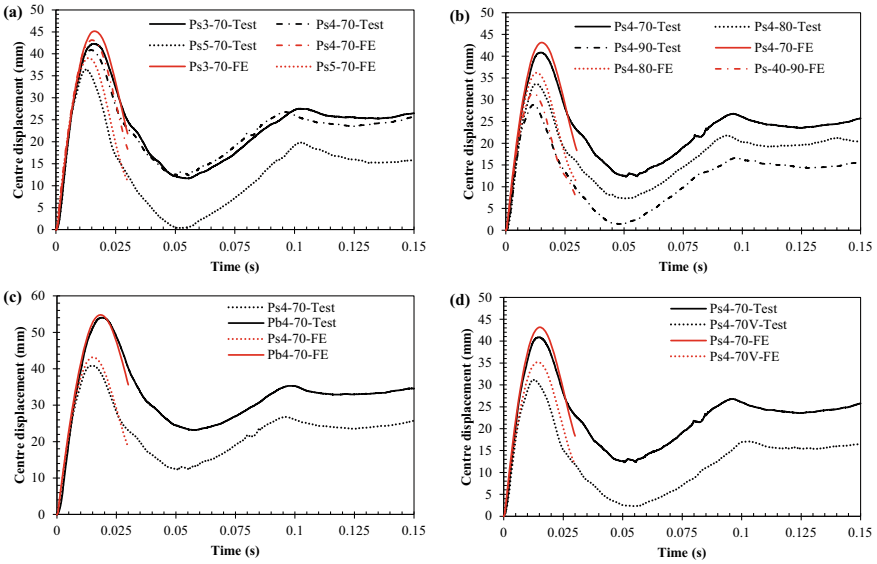

Fig. 6.28 Center displacement–time histories of test specimens: effects of **a** steel plate thickness, **b** concrete core thickness, **c** presence of stiffener, and **d** drop height, reprinted from Wang et al. (2022), copyright 2022, with permission from Elsevier

Displacement Response

The center displacement–time histories of the seven specimens are given in Fig. 6.28, and the corresponding maximum displacements are summarized in Table 6.6. During the experiments, when the drop hammer impact was applied on the panels, no detachment between panels and supports were observed during the loading process (i.e., up to the maximum displacement). However, the panels uplifted from the support during the unloading process due to the rebound, which can also be noticed in Fig. 6.28. After the rebound, the displacement of the panels became stable. The effect of steel plate thickness on the displacement–time histories are shown in Fig. 6.28a, and both the maximum and permanent displacements exhibit decrease with the increase of steel plate thickness, owing to the enhanced impact resistance of the panel. Table 6.6 indicates that the maximum center displacement of the panel is reduced by 3.40 and 16.00%, respectively, on increasing the thickness of steel plate from 2.84 mm to 3.52 and 4.46 mm. Moreover, the deflection of the SESCS sandwich panel is found to be reduced as the concrete core thickness is increased owing to the improved stiffness and resistance of the panel, as illustrated in Fig. 6.28b. Table 6.6 reveals that the maximum center displacement is reduced from 40.87 mm to 33.63 and 28.85 mm (by 21.52 and 41.66%), respectively, on increasing concrete core thickness from 70 mm to 80 and 90 mm. Figure 6.28c indicates that the SESCS sandwich panel with the presence of stiffeners evidently outperforms the traditional SCS sandwich panel in resisting impact load. The maximum center displacement of Ps4-70 is reduced by

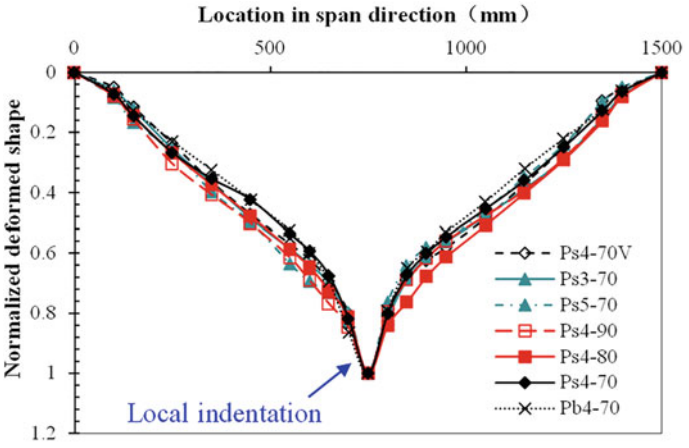

Fig. 6.29 Normalized deformed shapes of SESCS sandwich panels, reprinted from Wang et al. (2022), copyright 2022, with permission from Elsevier

24.36% compared to that of Pb4-70. Figure 6.28d exhibits a reduction in the deflection of the panel due to decrease in drop height and impact energy, i.e., the maximum center displacement is reduced by 31.20% on decreasing drop height from 1.8 m to 1.4 m.

After the tests, the permanent deformed shapes of all the specimens were measured manually using a laser ranging device. Figure 6.29 presents the normalized deformed shapes of the tested specimens in span direction, which further demonstrates that the global flexural deformations of the panels are formed, along with local indentation in the impact zone.

Energy Absorption Response

Among the seven tested specimens, six of them were subjected to the same impact energy with mass of hammer and drop height of 590 kg and 1.8 m. But, one specimen (PS4-70v) was tested with lesser impact energy (i.e., 590 kg mass of hammer and 1.4 m drop height). Energy–displacement curve is considered to evaluate and compare the energy absorption behavior of the proposed SESCS sandwich panel and traditional SCS sandwich panel under impact load. Also, the effects of concrete thickness, steel plate thickness and drop height on the energy absorption response of the SESCS panel are studied. Figure 6.30 presents the energy versus hammer displacement curves of the seven tested specimens, which are obtained by integrating the impact force with hammer displacement. It is noted that the energy absorbed by the panel almost exhibits a linear increase with the hammer displacement and reaches the peak value when the displacement of the hammer is maximum. A small fraction of the impact energy absorbed by the panel is released owing to the elastic recovery

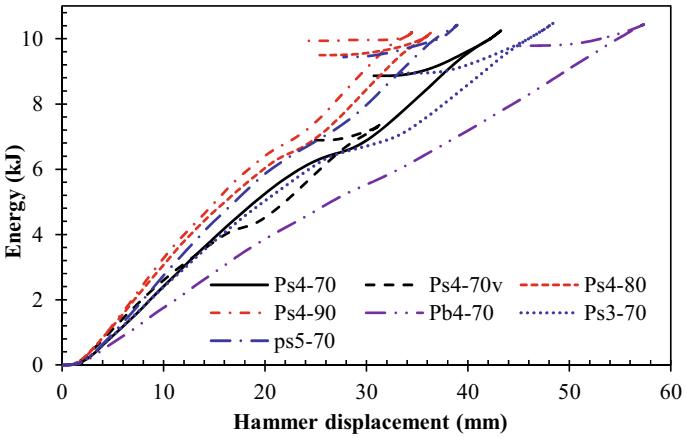

Fig. 6.30 Energy versus hammer displacement curve, reprinted from Wang et al. (2022), copyright 2022, with permission from Elsevier

of the steel and concrete material. It is also noted in Fig. 6.30 that the maximum energy absorbed by the panel subjected to the same impact energy is approximately the same. Moreover, the energy absorbing rate of the panel is found to be increased by increasing the thickness of concrete core and steel plate as well as employing the stiffeners, which also indicates an improved impact resistant performance.

6.3.2 Numerical Study

6.3.2.1 FE Model Establishment

The LS-DYNA software was used to carry out the numerical studies on the SESCS sandwich panels under impact loading. The half-symmetric FE model (shown in Fig. 6.31) was established owing to the symmetry of the specimen and loading condition. The element formulations, material models and properties, contact treatments and mesh sizes are consistent with those of SCS sandwich beams presented in Sect. 6.2.2.1.

6.3.2.2 Numerical Results and Discussions

The comparisons of impact force and displacement–time histories obtained from the tests and FE predictions are presented in Figs. 6.26 and 6.28, respectively. Figure 6.26 shows that the FE-predicted impact force–time histories match well with the test results for all the SESCS sandwich panels. The impact force–time histories from the FE simulations also experience three impact stages (i.e., inertial, loading,

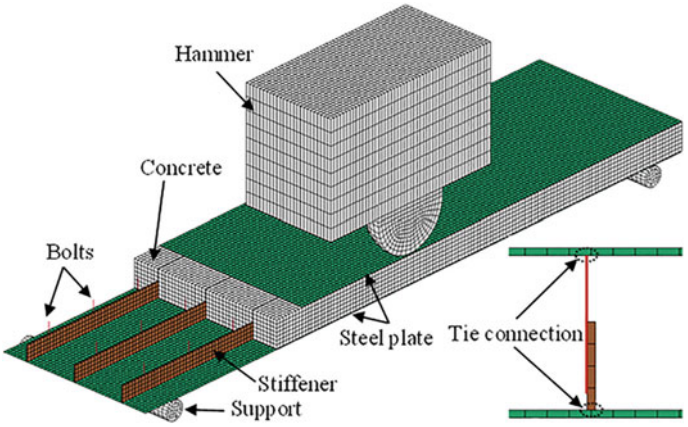

Fig. 6.31 Half-symmetric FE model of the SESCS sandwich panel, reprinted from Wang et al. (2022), copyright 2022, with permission from Elsevier

and unloading stages), similar to the test results. Likewise, the FE-predicted center displacement–time histories of the panels are also well matched with the test data, as shown in Fig. 6.28. Table 6.7 presents the comparison of FE predictions and test results in terms of peak impact force and maximum center displacement. The difference between the FE predictions and test results for peak impact force is found to be less than 7%, and the average ratio of FE to test for peak impact force is 0.96 with a coefficient of variation (COV) of 0.059. With regard to the maximum center displacement, its difference between the FE predictions and test results is less than 13%, and the average ratio of FE to test for maximum center displacement is 1.07 with a COV of 0.033. From the above comparisons of impact force and displacement responses between the FE predictions and test results, the accuracies of the established FE models can be validated.

Table 6.7 Comparison of FE predictions with test results

Specimen	F_{maxFE} (kN)	F_{maxFE}/F_{max}	D_{mmFE} (mm)	D_{mmFE}/D_{mm}
Ps4-70	349.82	0.93	43.14	1.06
Ps3-70	330.22	0.93	45.18	1.07
Ps5-70	386.03	1.00	39.06	1.07
Ps4-80	408.30	0.91	36.18	1.08
Ps4-90	456.48	0.96	31.51	1.09
Pb4-70	245.15	0.93	54.77	1.01
Ps4-70 V	309.64	1.07	35.20	1.13
Average	–	0.96	–	1.07
COV	–	0.059	–	0.033

Note The parameters with *FE* as the subscript stand for the FE predictions

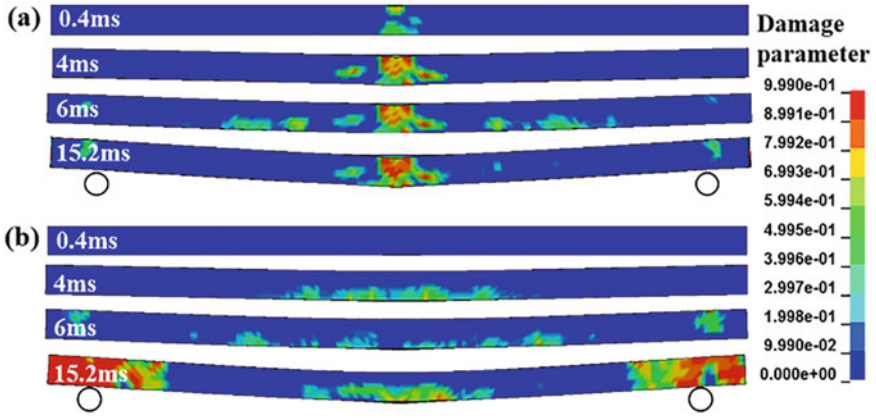

Fig. 6.32 Damage evolution of concrete core during impact: **a** Cross-section at impact point, **b** Cross-section at free side, reprinted from Wang et al. (2022), copyright 2022, with permission from Elsevier

The validated FE model was employed to reveal the damage evolution of concrete core during impact, and Fig. 6.32 presents the damage contours of concrete core at different times. The concrete core at impact zone immediately experiences local damage once being struck by the drop hammer, as it can be seen in Fig. 6.32a at 0.4 ms. At this moment, the damage of concrete is not observed at the free side of the panel (see Fig. 6.32b at 0.4 ms). Subsequently, local punching shear failure of the concrete core at impact zone can be observed at 4 ms, whereas flexure-induced damage of concrete at the free side of the panel can be observed with damage of concrete only appearing at the bottom surface (refer to Fig. 6.32b at 4 ms). The damage of concrete above the support occurs at 6 ms, and the concrete core exhibits increasingly severe damage with further collision. The maximum deflection of the panel is reached at 15.2 ms, and corresponding damage contours of the concrete core are also presented in Fig. 6.32. Punching shear failure of the concrete core at impact zone is evident, and the severe damage of concrete core at the free side of the panel occurs at mid-span and support owing to the large sagging moment at mid-span and reaction force at the support, respectively.

6.3.2.3 Parametric Studies

The influences of limited parameters on the impact resistance of the SESCS sandwich panels were explored experimentally. However, the design of panels may include several parameters to be considered for its use as an impact-resistant structural member. Hence, by employing the validated FE model, parametric studies were conducted to investigate the influence of various parameters on the impact responses of SESCS sandwich panels. The examined parameters were the impact velocity, hammer mass, impact energy (or initial kinetic energy), and momentum of the

hammer. One specimen (Psc) was selected as the reference specimen with same geometry and material properties to the specimen Ps4-70; two specimens (Psv5 and Psv7) were employed to study the effect of impact velocity; Psm3 and Psm9 were considered to investigate the influence of mass of hammer; the effect of impact energy was studied using Psk81 and Psk135 (while the identical momentum of the hammer was kept by selecting different combinations of impact velocity and hammer mass); the influence of momentum of the hammer was explored through Psp18 and Psp54 (while keeping the identical kinetic energy of the hammer by selecting different combinations of impact velocity and hammer mass). The details of the specimens for parametric studies and results are listed in Table 6.8.

The effects of impact velocity on the peak impact force, post-peak mean force and maximum center displacement of the SESCS sandwich panel are depicted in Fig. 6.33a. With the increase in impact velocity from 5 m/s to 6 and 7 m/s, the peak impact force is increased by 14.69 and 24.49%, respectively. Likewise, the corresponding increase of post-peak mean force is 16.16 and 24.77%, as listed in Table 6.8. This is because of the increase in kinetic energy associated with the higher impact velocity applied on the panels. Moreover, the increased impact velocity also increases the maximum center displacement, which can also be attributed to the improved impact energy. The maximum center displacement of the SESCS sandwich panel is increased by 26.00 and 58.32%, respectively, on increasing the impact velocity from 5 m/s to 6 and 7 m/s (or increasing the impact energy by 44 and 96%). It is noted that the increase in percentage of maximum center displacement is smaller than that of impact energy, which can be attributed to the improved post-peak mean force with the increase in the impact velocity. The energy–hammer displacement curves in Fig. 6.34a exhibit a noticeable rise in the maximum energy absorption and hammer displacement with the increase in the impact velocity. Moreover, evidently higher energy absorbing rate (i.e., the slope of energy versus hammer displacement curve) can be observed for the SESCS sandwich panel subjected to higher impact velocity when the hammer displacement exceeds around 10 mm.

Table 6.8 Summaries of numerical results

Specimen	v (m/s)	m (kg)	k (kJ)	p (kg·m/s)	F_{max} (kN)	F_m (kN)	D_{mm} (mm)
Psc	6.0	600	10.8	3600	367.00	219.84	43.98
Psv5	5.0	600	7.5	3000	319.98	189.25	34.90
Psv7	7.0	600	14.7	4200	398.35	236.14	55.26
Psm3	6.0	300	5.4	1800	327.35	145.36	26.04
Psm9	6.0	900	16.2	5400	368.21	245.61	58.90
Psk81	4.5	800	8.1	3600	289.30	198.68	37.58
Psk135	7.5	480	13.5	3600	403.77	229.30	51.12
Psp18	12	150	10.8	1800	438.71	255.23	38.42
Psp54	4.0	1350	10.8	5400	313.35	213.70	45.54

Note v, m, k, p–Impact velocity, hammer mass, kinetic energy and momentum of the hammer

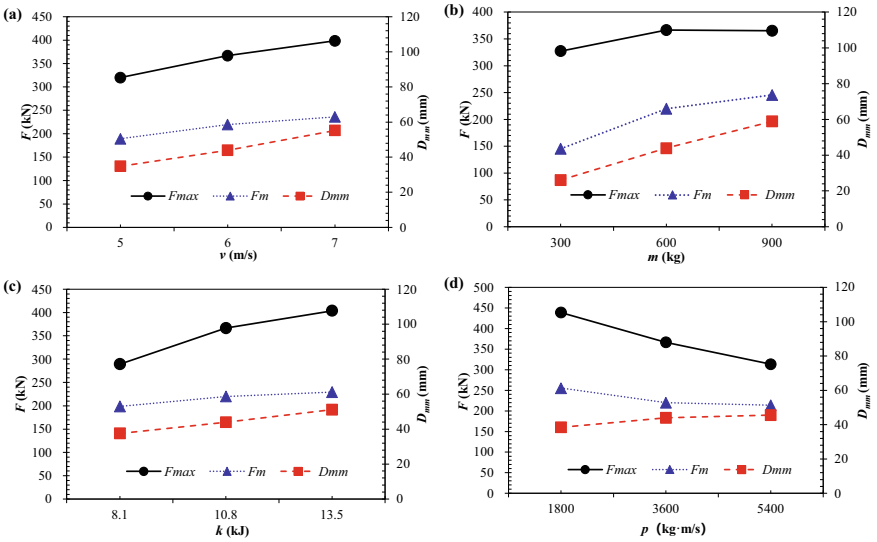

Fig. 6.33 Effects of **a** impact velocity, **b** hammer mass, **c** kinetic energy and **d** momentum of the hammer on the peak impact force, post-peak mean force and maximum center displacement, reprinted from Wang et al. (2022), copyright 2022, with permission from Elsevier

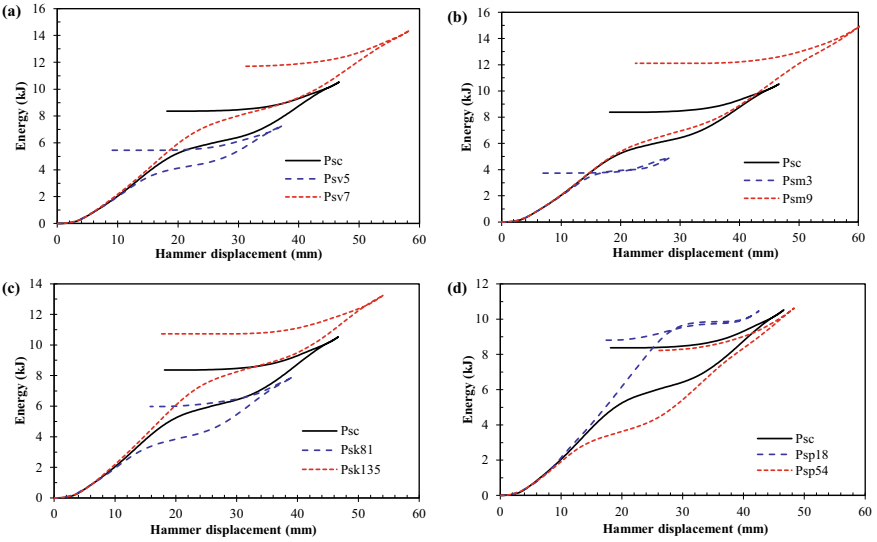

Fig. 6.34 Effects of **a** impact velocity, **b** hammer mass, **c** kinetic energy, and **d** momentum of the hammer on the energy–hammer displacement curves, reprinted from Wang et al. (2022), copyright 2022, with permission from Elsevier

Figure 6.33b presents the influence of mass of hammer on the peak impact force, post-peak mean force and maximum center displacement of the SESCS sandwich panel. The increase in the hammer mass from 300 kg to 600 and 900 kg shows a limited influence on the peak impact force of the SESCS sandwich panel (i.e., increase by 12.11 and 12.48%, respectively). However, a noticeable increase of post-peak mean force by 51.24 and 68.97% is observed owing to the higher impact energy applied on the panel. Moreover, increasing hammer mass from 300 kg to 600 and 900 kg also leads to 68.89% and 126.19% increase in the maximum center displacement, which is also due to the significantly increased impact energy (by 100% and 200%). Likewise, the increase in magnitude of maximum center displacement is less significant as compared to the improvement of impact energy. The influence of increase in hammer mass on the energy absorption behavior of the SESCS sandwich panel is found to be similar to the influence of increasing impact velocity, as presented in Fig. 6.34b.

Figure 6.33c presents the effect of impact energy on the impact response of the SESCS sandwich panel. Herein, the same momentum of the hammer is kept by varying both the impact velocity and hammer mass, as presented in Table 6.8. It is noted in Fig. 6.33c that the peak impact force, post-peak mean force and maximum center displacement exhibit increase with the increase of impact energy, which is consistent with the effects of impact velocity and hammer mass on the impact response of the SESCS sandwich panel. The peak impact force, post-peak mean force and maximum center displacement are increased by 39.56%, 15.41% and 36.03%, respectively, on increasing the impact energy from 8.1 to 13.5 kJ (by 66.67%). Energy–hammer displacement curves plotted in Fig. 6.34c also demonstrates that the energy absorbed by the SESCS sandwich panel increases with the increase in the applied impact energy (or initial kinetic energy). Higher applied impact energy results in higher peak impact force and post-peak mean force, which also leads to an increased energy absorbing rate of the SESCS sandwich panel.

The influence of momentum of the hammer on the impact response of the SESCS sandwich panel is presented in Fig. 6.33d. Herein, the same impact energy of the hammer is kept by varying both the impact velocity and hammer mass, as listed in Table 6.8. The peak impact force in Fig. 6.33d exhibits an evident decrease (by 16.34 and 28.57%, respectively) by increasing the momentum of the hammer from 1800 kg·m/s to 3600 and 5400 kg·m/s. This is mainly caused by the reduced impact velocity, i.e., the impact velocity is reduced from 12 m/s to 6 and 4 m/s. This indicates that the peak impact force is more sensitive to the impact velocity, which is consistent with the observation from Fig. 6.33a. Figure 6.33d also indicates that the increase of momentum leads to the reduction of post-peak mean force, but the increase of maximum center displacement. Although the same impact energy is applied on the SESCS sandwich panel, the reduced impact velocity may result in a smaller strain rate and resistance of the panel. Hence, lower post-peak mean force and higher maximum center displacement are observed for the panel subjected to the impact with a higher momentum (or smaller impact velocity). The energy versus hammer displacement curves in Fig. 6.34d also shows that the energy absorbed by the panels is approximately the same owing to the identical applied impact energy. In addition,

the energy absorbing rate is found to be reduced by increasing momentum of the hammer owing to the reduced post-peak mean force.

6.4 Summary

A new SCS sandwich structure enhanced with stiffeners in the tension plate (i.e., SESCS sandwich structure) was proposed for impact resisting. The impact responses of SESCS sandwich beams and panels were studied and presented in this chapter. The main findings are summarized as follows:

(1) All the SESCS sandwich beams exhibited flexural failure modes with evident plastic hinges located at their mid-spans, which resulted in vertical cracks and crushing of concrete in the tension and compression zone, respectively. Some slippages between the bottom plate and concrete core were observed, which could be caused by the vertical and diagonal cracks near the support. Experimental results revealed that the impact resistance of the SESCS sandwich beam was significantly improved as compared to the SCS sandwich beam with bolt connectors.

(2) The impact resistance of the SESCS sandwich beam was found to be improved by increasing concrete core and faceplate thickness in terms of larger post-peak mean force and smaller deflection.

(3) Numerical studies on the SESCS sandwich beam under impact loading were conducted, and the damage evolution of the concrete core during impact was revealed. Moreover, the whole cross-section of the stiffener at the mid-span was found to yield, which demonstrated the effective enhancement of the stiffener to the bending resistance of the beam. An analytical model based on the equivalent SDOF system was proposed for predicting the displacement response of the SESCS sandwich beam under impact loading, and reasonable predictions from the analytical model was demonstrated.

(4) All the SESCS sandwich panels exhibited the combined deformation mode of global flexure and location indentation, and three types of concrete cracks were observed, including vertical cracks at mid-span, diagonal cracks near the support, and vertical cracks above the support.

(5) The proposed SESCS sandwich panels with stiffeners in tension plate exhibited superior impact resistance compared to the traditional SCS sandwich panel in terms of higher peak impact force and post-peak impact force as well as smaller deformation. The maximum displacement of the SESCS sandwich panel was reduced by 36.90% on increasing the thickness concrete core by 20 mm, and there was a reduction of 15.67% by increasing the steel plate thickness from 2.84 to 4.46 mm.

(6) The damage evolution of concrete core of the SESCS sandwich panel during impact was revealed. Punching shear failure of concrete core was observed at

the impact zone, whereas flexure-induced damage of concrete at the free side of the panel was observed.

(7) Parametric studies indicated that the peak impact force was more sensitive to the impact velocity. The post-peak mean force was found to be increased by increasing the impact velocity and mass of hammer. The maximum displacement of the SESCS sandwich panel was slightly increased by increasing the momentum of the hammer even though the same impact energy was applied on the panel.

References

Abramowicz W, Jones N (1986) Dynamic progressive buckling of circular and square tubes. Int J Impact Eng 4:243–270

ASCE/SEI 59-11 (2011) Blast protection of buildings. American Society of Civil Engineers, Reston, Virginia

Biggs JM (1964) Introduction to structural dynamics. McGraw-Hill, New York

Chen W, Hao H, Chen S (2015) Numerical analysis of prestressed reinforced concrete beam subjected to blast loading. Mater Des 65:662–674

Clubley S K, Moy SSJ, Xiao RY (2003) Shear strength of steel-concrete-steel composite panels. Part I–testing and numerical modelling. J Constr Steel Res 59:781–794

Dogan O, Roberts TM (2012) Fatigue performance and stiffness variation of stud connectors in steel-concrete-steel sandwich systems. J Constr Steel Res 70:86–92

Eurocode 4 (2004a) Design of composite steel and concrete Structures–Part 1.1: General rules and rules for buildings, BS EN 1994–1–1, London

Eurocode 2 (2004b) Design of concrete structures–Part 1–1: General rules and rules for buildings, BS EN 1992–1–1, London

Federal Highway Administration (2007a) Evaluation of LS-DYNA concrete material model 159

Federal Highway Administration (2007b) Users manual for LS-DYNA concrete material model 159

Foundoukos N (2005) Behavior and design of steel-concrete-steel sandwich construction. Dissertation, University of London

Gu X, Jin X, Zhou Y (2015) Basic principles of concrete structures. Tongji University Press, Shanghai

Guo YT, Chen J, Nie X et al (2020) Investigation of the shear resistance of steel-concrete-steel composite structures with bidirectional webs. J Constr Steel Res 164:105846

Guo Q, Zhao W (2019a) Design of steel-concrete composite walls subjected to low-velocity impact. J Constr Steel Res 154:190–196

Guo Q, Zhao W (2019b) Displacement response analysis of steel-concrete composite panels subjected to impact loadings. Int J Impact Eng 131:272–281

Hallquist JO (2013) LS-DYNA keyword user's manual. Livermore Software Technology Corporation (LSTC). Livermore, California

Hallquist JO (2006) LS-DYNA theory manual. Livermore Software Technology Corporation (LSTC). Livermore, California

Li X, Chen JF, Lu Y et al (2015) Modelling static and dynamic FRP-concrete bond behavior using a local concrete damage model. Adv Struct Eng 18(1):45–58

Liew JYR, Sohel KMA (2009) Lightweight steel-concrete-steel sandwich system with J-hook connectors. Eng Struct 31:1166–1178

Liew JYR, Sohel KMA, Koh CG (2009) Impact tests on steel–concrete–steel sandwich beams with lightweight concrete core. Eng Struct 31(9):2045–2059
Liew JYR, Sohel KMA, Koh CG (2015) Numerical modeling of lightweight steel-concrete-steel sandwich composite beams subjected to impact. Thin-Walled Struct 94:135–146
Lu J, Wang Y, Zhai X (2021) Response of flat steel-concrete-corrugated steel sandwich panel under drop-weight impact load by a hemi-spherical head. J Build Eng 44:102890
Nie JG, Ma XW, Tao MX et al (2014) Effective stiffness of composite shear wall with double plates and filled concrete. J Constr Steel Res 99:140–148
Oduyemi TOS, Wright HD (1989) An experimental investigation into the behavior of double skin sandwich beams. J Constr Steel Res 14(3):197–220
Remennikov AM, Kong SY (2012) Numerical simulation and validation of impact response of axially-restrained steel-concrete-steel sandwich panels. Compos Struct 94(12):3546–3555
Remennikov AM, Kong SY, Uy B (2013) The response of axially restrained non-composite steel-concrete-steel sandwich panels due to large impact loading. Eng Struct 49:806–818
Shariati M, Ramli Sulong NH, Arabnejad Khanouki MM (2012) Experimental assessment of channel shear connectors under monotonic and fully reversed cyclic loading in high strength concrete. Mater Des 34:325–331
Shariati M, Ramli Sulong NH, Shariat A et al (2013) Comparison of behaviour between channel and angle shear connectors under monotonic and fully reversed cyclic loading. Constr Build Mater 38:582–593
Shariati M, Ramli Sulong NH, Shariat A et al (2016) Comparative performance of channel and angle shear connectors in high strength concrete composites: an experimental study. Constr Build Mater 120:382–392
Sohel KMA, Liew JYR (2014) Behavior of steel–concrete–steel sandwich slabs subject to impact load. J Constr Steel Res 100:163–175
Sohel KMA, Liew JYR, Alwis WAM et al (2003) Experimental investigation of low-velocity impact characteristics of steel-concrete-steel sandwich beams. Steel Compos Struct 3(4):289–306
Subedi NK, Coyle NR (2002) Improving the strength of fully composite steel-concrete-steel beam elements by increased surface roughness–an experimental study. Eng Struc 24:1349–1355
Thang V, Marshall P, Brake NA et al (2016) Studded bond enhancement for steel-concrete-steel sandwich shells. Ocean Eng 124:32–41
Wang Y, Liew JYR, Lee SC (2015a) Theoretical models for axially restrained steel-concrete-steel sandwich panels under blast loading. Int J Impact Eng 76:221–231
Wang Y, Lu J, Liu S et al (2021) Behaviour of a novel stiffener-enhanced steel–concrete–steel sandwich beam subjected to impact loading. Thin-Walled Struct 165:107989
Wang Y, Qian X, Liew JYR et al (2014) Experimental behavior of cement filled pipe-in-pipe composite structures under transverse impact. Int J Impact Eng 72:1–16
Wang Y, Qian X, Liew JYR et al (2015b) Impact of cement composite filled steel tubes: An experimental, numerical and theoretical treatise. Thin-Walled Struct 87:76–88
Wang Y, Sah TP, Liu S et al (2022) Experimental and numerical studies on novel stiffener-enhanced steel-concrete-steel sandwich panels subjected to impact loading. J Build Eng 45:103479
Wang Y, Zhai, X, Lee SC et al (2016) Response of curved steel-concrete-steel sandwich shells subjected blast loading. Thin-Walled Struct 108:185–192
Wang Z, Yan J, Liu Y et al (2020) Mechanical properties of steel-UHPC-steel slabs under concentrated load considering composite action. Eng Struct 222:111095
Xie M, Foundoukos N, Chapman J.C (2007) Static tests on steel-concrete-steel sandwich beams. J Constr Steel Res 63(6):735–750
Yan C, Wang Y, Zhai X (2020a) Low velocity impact performance of curved steel-concrete-steel sandwich shells with bolt connectors. Thin-Walled Struct 150:106672
Yan C, Wang Y, Zhai X et al (2020b) Strength assessment of curved steel-concrete-steel sandwich shells with bolt connectors under concentrated load. Eng Struct 212:110465
Yan JB, Guan H, Wang T (2020c) Steel-UHPC-steel sandwich composite beams with novel enhanced C-channel connectors: Tests and analysis. J Constr Steel Res 170:106077

Yan JB, Hu H, Wang T (2020d) Shear behavior of novel enhanced C-channel connectors in steel-concrete-steel sandwich composite structures. J Constr Steel Res 166:105903

Yan JB, Liew JYR, Zhang MH et al (2015) Experimental and analytical study on ultimate strength behaviour of steel-concrete-steel sandwich composite beam structures. Mater Struct 48(5):1523–1544

Zhao W, Guo Q (2018) Experimental study on impact and post-impact behavior of steel-concrete composite panels. Thin-Walled Struct 130:405–413

Zhao W, Guo Q, Dou X et al (2018) Impact response of steel-concrete composite panels: Experiments and FE analyses. Steel Compos Struct 26(3):255–263